Transcriptomic Signatures of WNT-Driven Pathways and Granulosa Cell-Oocyte Interactions during Primordial Follicle Activation

Hinako M. Takase[1,5]*, Tappei Mishina[1,2,5], Tetsutaro Hayashi[3,4], Mika Yoshimura[3], Mariko Kuse[3], Itoshi Nikaido[3,4], Tomoya S. Kitajima[1]

[1]Laboratory for Chromosome Segregation, RIKEN Center for Biosystems Dynamics Research (BDR), Kobe, Japan.

[2]Faculty of Agriculture, Kyushu University, Fukuoka, Japan.

[3]Laboratory for Bioinformatics Research, RIKEN Center for Biosystems Dynamics Research (BDR), Kobe, Japan.

[4]Department of Functional Genome Informatics, Division of Biological Data Science, Medical Research Institute, Tokyo Medical and Dental University (TMDU), Bunkyo, Japan.

[5]These authors contributed equally to this research.

*Author for Corresponding author:

Email: hinako.takase@riken.jp (HT)

Abstract

Primordial follicle activation (PFA) is a pivotal event in female reproductive biology, coordinating the transition from quiescent to growing follicles. This study employed comprehensive single-cell RNA sequencing to gain insights into the detailed regulatory mechanisms governing the synchronized dormancy and activation between granulosa cells (GCs) and oocytes with the progression of the PFA process. *Wntless* (*Wls*) conditional knockout (cKO) mice served as a unique model, suppressing the transition from pre-GCs

to GCs, and disrupting somatic cell-derived WNT signaling in the ovary. Our data revealed immediate transcriptomic changes in GCs post-PFA in *Wls* cKO mice, leading to a divergent trajectory, while oocytes exhibited modest transcriptomic alterations. Subpopulation analysis identified the molecular pathways affected by WNT signaling on GC maturation, along with specific gene signatures linked to dormant and activated oocytes. Despite minimal evidence of continuous up-regulation of dormancy-related genes in oocytes, the loss of WNT signaling in (pre-)GCs impacted gene expression in oocytes even before PFA, subsequently influencing them globally. The infertility observed in *Wls* cKO mice was attributed to compromised GC-oocyte molecular crosstalk and the microenvironment for oocytes. Our study highlights the pivotal role of the WNT-signaling pathway and its molecular signature, emphasizing the importance of intercellular crosstalk between (pre-)GCs and oocytes in orchestrating folliculogenesis.

Author summary

In mammalian ovaries, primordial follicles protect dormant oocytes from wasteful consumption. We explored the complex molecular dynamics of the critical process of primordial follicle activation (PFA) that underlies female reproductive health, with a focus on the role of WNT signaling. By utilizing a unique mouse model with disrupted WNT signaling, our study reveals novel insights into the regulatory dynamics of granulosa cells (GCs) and oocytes during PFA. Single-cell transcriptome profiling uncovered distinct cell populations and highlighted the impact of WNT signaling on ovarian cell types. This study reveals distinct transcriptomic changes in GCs post-PFA, which affects their differentiation trajectories and highlights the critical role of WNT signaling in establishing GC function. We further examined the consequences of disrupted microenvironments on oocytes and GC-oocyte interactions, which elucidated altered oocyte subclusters and potential links to infertility. These findings provide a foundation for understanding the connections between WNT signaling and ovarian function. Our comprehensive analysis contributes valuable knowledge to reproductive biology, emphasizing the clinical relevance of WNT signaling in female fertility.

Introduction

Folliculogenesis is a strictly controlled and dynamic process that is essential for the success of female reproduction. The formation of primordial follicles occurs shortly after birth in mice [1], with characteristic flattened pre-granulosa cells (pre-GCs) encompassing each oocyte individually [2]. Primordial follicles are particularly important in determining ovarian reserves, serving as a pool of dormant oocytes. A subset of primordial follicles undergoes activation, initiating the irreversible process of folliculogenesis. During primordial follicle activation (PFA) to become primary follicles, pre-GCs develop into cuboidal and proliferative granulosa cells (GCs) and simultaneously oocytes start to grow [3,4]. Subsequent stages of folliculogenesis include secondary follicles, antral follicles and preovulatory follicles, with only a limited number of oocytes reaching ovulation. This continuous process of folliculogenesis is repeated throughout the reproductive period until menopause. Since the failure of PFA can lead to an inadequate or a transiently excessive supply of oocytes, the precise regulation of PFA is imperative for successful reproduction [5,6]. Anomalies in PFA are believed to contribute to premature ovarian insufficiency in humans [7]. Nonetheless, how primordial follicle quiescence and activation are regulated is incompletely understood.

PFA is an orchestrated process of somatic cells and oocytes, with bidirectional communication between them being crucial. Therefore, it is important to understand the intricate control of the dynamic states of both GCs and oocytes during PFA. To date, several key molecular components that regulate PFA have been identified. The maintenance of oocyte dormancy relies on the nuclear localization of the transcription factor forkhead box O3 (FOXO3), a reliable indicator of PFA [6,8]. In oocytes, FOXO3 is phosphorylated and translocated to the cytoplasm via the PI3K-AKT signaling pathway followed by KIT signal transduction, in response to GC-derived ligands which leads to PFA [9]. It is also known that oocyte-derived GDF9 promotes GC cell proliferation [10] and the mTORC1 pathway in pre-GCs contributes to PFA [11]. In addition, environmental factors such as hypoxia, extracellular matrix (ECM)-mediated pressure and nutritional factors have been identified as crucial components in the maintenance of primordial follicles [12,13]. The oocyte surrounding microenvironments provided by pre-GCs are dynamically

75 changed during PFA associated with GC maturation. Despite research efforts on the molecular components
76 that govern PFA, the complexities of GC-oocyte communication and their dynamic states has remained
77 elusive.

78 We and other research groups have reported the significant role of WNT signaling in postnatal
79 folliculogenesis in mice. Interestingly, according to a study by De Cian *et al.*, the oocyte-GC interaction is
80 also key here, as oocyte-derived RSPO2, a positive regulator of WNT signaling, acts on neighboring GCs
81 [14]. In contrast, our research revealed an autocrine function of WNT signaling in pre-GCs during PFA to
82 permit transformation to GCs. In *Wls* cKO mice, in which somatic cell-derived WNT secretion is
83 suppressed, pre-GCs fail to acquire GC properties upon PFA stimulation, remaining flat, with less
84 cytoplasm and with low cell proliferative activity [15]. Despite the simultaneous activation expected for
85 GCs and oocytes, they failed to synchronize in *Wls* cKO mice - only the oocytes grow and increased in size.
86 However, these oocytes exhibited some immature characteristics such as possible retained dormancy as
87 indicated by the nuclear localization of FOXO3. Since these results suggest that oocyte awakening requires
88 support from functional GCs, *Wls* cKO mice emerge as a valuable tool for investigating the unidentified
89 role of GCs in this context.

90 In this study, we aimed to advance foundational knowledge about folliculogenesis and infertility
91 by uncovering the single-cell resolution regulatory dynamics during PFA using *Wls* cKO mice, expecting
92 that their novel phenotype would allow us to address the following questions: (i) What are the molecular
93 mechanisms by which cKO of *Wls* causes defective pre-GC to GC development? (ii) How does GC mis-
94 differentiation in *Wls* cKO mice affect the transcriptome of interacting oocytes? We tested the level of
95 oocyte autonomous gene regulation against WNT signaling dependent molecular crosstalk with GCs and/or
96 their poor surrounding environment. (iii) What is the molecular signature of the unsynchronized PFA
97 process in oocytes that grow despite the possible indication of retained dormancy? Since FOXO3 is
98 anticipated to function as a transcription factor in the nucleus, we investigated "dormancy genes" that are
99 continuously up-regulated even in growing oocytes in *Wls* cKO mice.

100 The results show that cKO of *Wls* caused immediate transcriptomic changes in GCs after PFA,

101 resulting in a divergent transcriptome trajectory, while oocytes exhibited modest transcriptome changes. In
102 oocytes of *Wls* cKO mice, although there was little evidence of the continuous up-regulation of "dormancy
103 genes" after PFA, the loss of WNT signaling in (pre-)GCs impacted some genes even before PFA, and
104 subsequently affected them globally, leading to infertility likely due to molecular crosstalk and a poor
105 surrounding environment. Thus, our data highlight the critical role of the WNT-signaling pathway and its
106 molecular signature in regulating normal follicular development.
107

108 Results

109 Ovaries of *Wls* cKO mice show abnormalities in GCs after PFA

110 The process of primordial follicle assembly in mice takes place from before birth to postnatal day (PD) 5,
111 followed by the growth of activated primordial follicles starting from PD6 [16–18]. Ovarian samples were
112 collected from wild-type and from *Wls* cKO mice at PD7, with an assumption that the cell populations
113 around the transition from primordial to primary follicles were abundantly present. Subsequently, we
114 conducted fluorescent immunostaining for an oocyte marker, DDX4, and confirmed the presence of
115 primordial, primary and small secondary follicles in control ovaries (Fig 1A). In contrast, *Wls* cKO ovaries
116 contained primordial follicles that appeared normal and primary follicles surrounded by abnormal GCs,
117 which was characterized by the absence of cuboidal and organized GC layers. To quantitatively evaluate
118 the phenotype of *Wls* cKO mice at PD7, we examined the thickness of the GC layer as well as the size of
119 oocytes by employing PAS staining of ovarian sections. An analysis of covariance (ANCOVA) detected a
120 significant disparity in GC thickness between control and *Wls* cKO mice. (Fig 1B). These differences
121 primarily reflect changes in the state of follicles after activation, as both regression lines are close for
122 primordial follicles with diameters less than 20 μm. The underdevelopment of the GC phenotype becomes
123 more prominent at a later stage of folliculogenesis [15]. These results indicate that control and *Wls* cKO
124 mice provide contrasting models to investigate the molecular mechanisms of PFA, and that ovaries at PD7
125 offer an optimal window for examining PFA.

126

127 **Single-cell transcriptome profiling of ovarian cells from *Wls* cKO mice and**
128 **from control mice identify different cell types**

129 To investigate cell type-specific alterations in gene expression during PFA with or without WNT-signaling,
130 we performed scRNA-seq analysis on the ovaries of control mice and *Wls* cKO mice at PD7 using RamDA-
131 seq, a full-length total RNA-sequencing method for single cells [19]. For these analyses, to obtain ovarian
132 somatic cells by flow cytometry, we utilized mice expressing red fluorescence (tdTomato) driven by
133 *Sf1(Nr5a1)*-Cre. Our cryosection analysis revealed the ubiquitous expression of tdTomato in ovarian
134 component cells, including GCs, while DDX4-positive oocytes were tdTomato-negative (Fig 1C).
135 tdTomato-positive somatic cells and KIT-positive oocytes were sorted from PD7 *Wls* cKO mice (*Sf1-*
136 *Cre;Wls*$^{flox/del}$*;Ai9*) and from their littermate controls (*Sf1-Cre;Wls*$^{flox/+}$*;Ai9*) by cell sorting (Fig S1A and
137 S1B). We obtained the high-quality transcriptome of 286 somatic cells and 95 oocytes collected from
138 control mice and from *Wls* cKO mice (Fig 1D). After stringent sequence quality filtration, a total of 721
139 cells were used for the analysis.

140 To characterize the ovarian cell type during PFA, the control and *Wls* cKO datasets were analyzed
141 separately. Seurat-based unsupervised clustering and visualization with uniform manifold approximation
142 and projection (UMAP) identified 6 and 7 clusters in the control and *Wls* cKO datasets, respectively,
143 demonstrating substantial differences in those cell populations (Fig 2A and 2B). The top 20 differentially
144 expressed genes (DEGs) for each cluster (Fig 2C, 2D, Table S1 and Table S2) were used to identify
145 corresponding known cell types based on the expression patterns of the included known cell type-specific
146 markers for each cluster on UMAP plots: for oocytes (*Ddx4*), for GCs (*Amh*), for pre-GCs (*Smad3*), for
147 ovarian surface epithelia (OSE) (*Krt19*), for mesenchymal cells (*Col1a1*) and for early theca cells (eTCs)
148 (*Enpep*) (Fig 2E) [20,21]. Among the *Col1a1*-positive mesenchymal cells, those with a low expression of
149 *Enpep* were considered interstitial cells. These analyses successfully identified five distinct cell clusters in
150 the control group: pre-GCs, GCs, OSE, interstitial cells (Int), eTCs and single oocyte clusters (OOs) (Fig

151 2A). Consistent with a previous report [15], expression of *Amh* in the GC cluster was lower in *Wls* cKO
152 mice than in the control mice (Fig 2E). Notably, the *Wls* cKO ovaries exhibited an absence of the eTC
153 population, while two additional clusters were present in the GC lineage (altered (alt)-GCs) and in oocytes
154 (altered (alt)-OOs) (Fig 2B). The lack of an eTC population in *Wls* cKO ovaries aligns with the absence of
155 normal developing follicles, as theca cells are typically recruited around the secondary follicle stage. The
156 alt-GC cluster identified in *Wls* cKO samples was characterized by a moderate GC marker expression and
157 DEGs such as *Pdlim4* and *Hsd3b1* (Fig 2D and 2E). The alt-oocyte cluster in *Wls* cKO samples expressed
158 well-known oocyte-specific markers in the DEGs, such as *Zp3*, *Lhx8* and *Gdf9*, closely resembling the
159 overall gene expression patterns of the oocyte cluster (Fig 2D). Nevertheless, it exhibited lower values in
160 various quality assessments, including reduced ratios of reads mapping to the intronic region (percent
161 intron), decreased total reads and fewer detected genes compared to the oocyte cluster (Fig 2E and S1C–
162 D) (for details, see the oocyte subpopulation analysis below). Since oocytes in *Wls* cKO mice are genetically
163 normal, their growth is predicted to be hindered by their interaction with abnormal GCs. Altogether, we
164 identified six and seven different ovarian cell types for control and *Wls* cKO ovaries, respectively, including
165 altered cell maturation without WNT-signaling in GCs, and characterized the gene expression features of
166 each cell type.
167

168 Distinct subclusters in GC maturation and their molecular signatures

169 To investigate the GC development process during PFA, we conducted a subpopulation analysis of GCs by
170 integrating data from control (pre-GCs and GCs in Fig 2A) and from *Wls* cKO (pre-GCs, GCs and alt-GCs
171 in Fig 2B) cells. The samples from *Wls* cKO and control ovaries exhibit mostly non-overlapping
172 distributions on the UMAP dimensionality reduction, indicating a genotype-dependent developmental
173 trajectory (Fig 3A). That analysis identified six distinct subgroups with specific DEGs (referred as G1–G6
174 subclusters), which sheds light on GC lineage development during PFA (Fig 3B, 3C, 3D and Table S3).
175 Within the G1 subcluster, *Wls* cKO and control samples were closely positioned and comprised

176 both cell types (Fig 3A and 3B), indicating the successful integration of the two datasets. Notably, known
177 mature GC markers such as *Inhbb* and *Apoa4* were markedly down-regulated in this cluster (Fig 3E).
178 Conversely, *Smad3*, a gene associated with pre-GCs [20], was highly expressed, identifying this subcluster
179 as pre-GCs (Fig 3E). Additionally, a proliferation marker *Top2a* was downregulated in this subcluster,
180 indicating a rather quiescent cell state (Fig 3E). Focusing on the trajectory of the control GCs, the highest
181 expression of the known GC markers *Vcan* and *Amh* in the G3 subcluster led to the assumption they are
182 mature GCs (GCs-Ctrl) (Fig 3D). The G2 subcluster displayed an intermediate gene expression between
183 pre-GCs and GCs-Ctrl, and therefore were presumed to be in the transition state (Transition-Ctrl).

184 Analogously, the G5 subcluster was designated as GC-cKO due to its higher expression of the
185 known GC markers *Inhbb* and *Apoa4* within the *Wls* cKO GC trajectory (Fig 3E). However, GCs-cKO does
186 not fully acquire the typical transcriptome properties of normal GCs, as indicated by the insufficient
187 expression of *Vcan* and *Amh*, suggesting an aberrant activation (Fig 3D). The G4 subcluster positioned
188 between GCs-cKO (G5) and pre-GCs (G1) was identified as Transition-cKO. Lastly, the G6 subcluster
189 exhibits the lowest expression of the pan-GC markers *Nr5a1* and *Amhr2* (Fig 3E). The underdevelopment
190 of GCs-cKO could lead to the altered GC (Alt-GCs; G6) subcluster characterized by marker genes linked
191 to stress responses, such as *Pdlim4* and *Clu* (Fig 3D). The consistent expression pattern of PDLIM4 was
192 observed by immunostaining of ovarian sections from control and from *Wls* cKO 3-week-old mice (Fig
193 3G). The results revealed a robust expression of PDLIM4 in GCs of secondary follicles in *Wls* cKO ovaries,
194 while a minimal expression of PDLIM4 was observed in the entire GC lineage of control ovaries. Therefore,
195 the Alt-GC subcluster in *Wls* cKO ovaries likely includes GCs from secondary follicles and their subsequent
196 developmental stages. Together, analysis of the subcluster distribution reveals that in *Wls* cKO ovaries, pre-
197 GCs undergo a distinct differentiation trajectory shortly after the PFA.

198 Note that the annotations for subclusters in this analysis, although some of them share identical
199 names, may not precisely match those in Fig 2 due to the finer classification. By comprehensively
200 examining markers for the broad GC lineage (*Kitl*, *Nr5a1* and *Amhr2*), the pre-GCs as depicted in Fig 2
201 (*Ano1* and *Bmp4*) and the mature GCs (*Inhbb* and *Apoa4*), we observed an expected but gradual variation

202 between subclusters (Fig 3E). We also observed the anticipated reduced production of WNT ligands (*Wnt4*,
203 *Wnt6* and *Wnt11*), which have been reported to be expressed in GC lineages, in *Wls* cKO subclusters (G3,
204 G4 and G6) [15]. Additionally, we noticed the inclusion of heat shock proteins (*Hspd1*, *Hspe1* and *Hsph1*)
205 specifically in the marker genes of the GC-Ctrl (G3) subgroup, suggesting a potential dependence on WNT
206 signaling for that response.

207 Next, we proceeded to examine the biological features of each identified subcluster using Gene
208 ontology (GO) analysis of DEGs. That analysis revealed the presence of distinct characteristics of GC cells
209 and illustrated the aberrant maturation pathway in *Wls* cKO ovaries (Fig 3F). For example, the pre-GC (G1)
210 subcluster exhibited GO terms and marker genes linked to cell migration and adhesion, indicating a unique
211 cellular behavior in pre-GCs as a common mechanism in the early stages of GC development. The
212 Transition-Ctrl (G2) subcluster did not yield significant GO terms, primarily due to the limited number of
213 DEGs. Nevertheless, a few marker genes related to calcium regulation and the ECM were identified, such
214 as *Cdh12* (Fig 3D). Although the Transition-cKO (G4) subcluster included GO terms related to the ECM,
215 such as "positive regulation of integrin-mediated signaling pathway", the most prominent term was
216 "endoplasmic reticulum to cytosol transport." This process is thought to be crucial for maintaining cellular
217 homeostasis by eliminating damaged proteins from the ER, suggesting a response to stressful environments.
218 The GC-Ctrl (G3) subcluster exhibited terms linked to cell proliferation and protein synthesis. In contrast,
219 the cell proliferation-related term was not significantly enriched in the GC-cKO (G5) subcluster, which is
220 consistent with our previous findings that *Wls* cKO GCs exhibited reduced proliferation [15]. Nevertheless,
221 the GC-cKO (G5) subcluster showed somewhat similar characteristics to the GC-Ctrl (G3) subcluster, such
222 as the enrichment of terms related to protein translation. The Alt-GC (G6) subcluster corresponded to the
223 Alt-GC cluster in the entire ovarian cell dataset of Fig 2 (Fig 3A). The Alt-GC (G6) subcluster is primarily
224 characterized by the GO terms of suppression of cellular movement and translation. While not statistically
225 significant in the GO term analysis, it came to our attention that the Alt-GC (G6) subcluster exhibited
226 elevated expression of hypoxia-related genes (*Foxo1*, *Trp53inp1* and *Hif1a*), implying a deteriorating
227 cellular environment (Fig 3E). Collectively, our analysis revealed a pivotal role for WNT signaling in the

228 rigorous transcriptome activation and subsequent maturation of GC lineages during PFA and depicted the
229 gene expression signatures for each GC type.
230

231 WNT-dependent and independent gene regulatory network during the 232 maturation of GCs

233 To further characterize differences and similarities between WNT-signaling dependent and independent
234 GC transcriptome activation during PFA, we conducted DEG analysis using the singleCellHaystack method
235 [22]. This approach allowed us to identify broader patterns of gene expression changes without relying on
236 the explicit clustering of cells. Based on the expression kinetics of the top 1,000 genes of the 4,156 DEGs
237 detected, our analysis identified four distinct DEG clusters (designated as clusters 1-4) after careful
238 evaluation (Fig 4A and Table S4). When clusterings with five or more groups were tested, they contained
239 additional clusters with subtle differences in expression kinetics (Fig S2). Thus, we inferred that four
240 clusters effectively represented the overview of the heterogeneity of expression kinetics. Clusters 1 and 2
241 showed similar expression kinetics between control and *Wls* cKO GCs, with the former and the latter genes
242 being up- and down-regulated, respectively, after the pre-GC activation (Fig 4A). Interestingly, these likely
243 WNT-signaling independent DEGs account for 81% of the highly DEGs (cluster 1: 536 genes, cluster 2:
244 274 genes). In contrast, clusters 3 and 4 had fewer DEGs (cluster 3: 101 genes, and cluster 4: 89 genes),
245 but showed contrasting regulation between control and *Wls* cKO GCs in the broad developmental stage of
246 GCs (Fig 4A). These results suggest that, even in *Wls* cKO GCs, the majority of the transcriptome profiles
247 associated with GC activation are still preserved. However, the absence of autocrine WNT-signaling
248 interferes with essential pathways crucial for proper GC development.

249 To elucidate the functional significance of the transcriptional profiles generated through the
250 singleCellHaystack-based clustering, we performed an enrichment analysis (Fig 4B and Table S5). That
251 analysis revealed a significant upregulation of pathways associated with GC activation, which were either
252 unaffected or affected by WNT signaling. Post-activation GCs (cluster 1) included GO terms linked to

253 active protein synthesis, regardless of the presence or absence of WNT signaling. In pre-GCs (cluster 2),
254 genes associated with cell-cell adhesion are highly expressed, which suggests that the maintenance of
255 plasma membrane integrity is important for their function. Our data also provide additional support for the
256 importance of ECM production by pre-GCs, which reinforces the notion that a rich ECM surrounding
257 primordial follicles is crucial for maintaining oocyte dormancy [13]. *Wls* cKO GC lineage (cluster 3)
258 contains GO terms such as "transmembrane receptor protein serine/threonine kinase signaling pathway"
259 and "positive regulation of cell differentiation". These up-regulated genes included those encoding proteins
260 related to activation of the TGFβ/BMP pathway (*Bmp2*, *Bmp4* and *TGFB1l1*) (Table S5). The inappropriate
261 intercellular signaling may lead to instability or incorrect cell lineage identity. Remarkably, in the control
262 GC lineage (cluster 4), genes associated with the maintenance of proteostasis and response to steroid
263 hormone stimulus were up-regulated, which appears to be a hallmark of functional GCs that require WNT
264 signaling.

265 Next, we investigated regulators of the pre-GC to GC transition-associated changes in gene
266 expression. We conducted gene co-expression analysis using GENIE3 [23] with the top 1,000 DEGs
267 identified through singleCellHaystack analysis. That analysis revealed core hub genes in GCs and their
268 expression kinetics during PFA in relation to WNT signaling (Fig 4C and 4D). *Nr5a2*, *Tcf7* and *Tox2*,
269 associated with cluster 1, were expressed in both *Wls* cKO and control GCs (Fig 4D). Those genes have
270 been reported to play critical roles in GC function and fate determination [24–26]. *Ets1* and *Irx3*, which are
271 enriched in cluster 2, were highly expressed in pre-GCs (Fig 4D). *Ets1* has been implicated in the
272 pathogenesis of polycystic ovary syndrome [27,28], while *Irx3* has been reported to be essential for oocyte
273 quality control through ECM production [29,30]. *Tsc22d1* and *Bmp2*, which are upregulated in cluster 3 of
274 *Wls* cKO GCs, have been linked to the TGFβ/BMP pathway, potentially affecting the failure of transition
275 from pre-GC to GC. *Fosb* is exclusively expressed in control GCs like cluster 4 (Fig 4D). The expression
276 of *Fosb* has been documented in GCs and in luteal cells, suggesting its involvement in GC differentiation
277 [31,32]. Immunostaining for the inferred hub regulator IRX3 validated the depicted expression kinetics,
278 showing higher expression in pre-GCs that decreased during the maturation process, with no notable

279 difference between control and *Wls* cKO groups (Fig 4E and 4F). Taken together, our analysis characterized
280 the molecular signature of unexpected similarities and key differences in the landscape of GC transcriptome
281 activation during PFA between the presence or absence of WNT signaling and identified their possible core
282 regulators.
283

284 Transcriptomic consequences in oocytes that are impacted by disrupted WNT 285 signaling and GC mis-differentiation

286 We then investigated the impact of disrupted WNT signaling on GC maturation on the oocyte transcriptome
287 during PFA. We conducted a subpopulation analysis by integrating data from both the control (Oocyte in
288 Fig 2A) and *Wls* cKO (Oocyte in Fig 2B) datasets, excluding the altered oocyte cluster from the analysis.
289 The clustering analysis with Seurat identified three distinct subclusters inferred as O1; Dormant, O2;
290 Activated-Ctrl, and O3; Activated-cKO (Fig 5A, 5B, 5C, and 5D). These subclusters were annotated
291 according to the known increased expression patterns of maternal genes associated with PFA, such as *Zp1*,
292 *Zp2*, *Zp3* and *Gdf9* (Fig 5E). The dormant cluster consisted of both control and *Wls* cKO mice-derived
293 oocytes (Fig 5B). Upon oocyte activation, we found a subtle change in gene expression patterns between
294 the control and *Wls* cKO samples, detecting a small number of DEGs that characterized each sub-cell type
295 (Dormant (O1): 61, Activated-Ctrl (O2): 316, Activated-cKO (O3): 10) (Table S6).
296 Prior to a detailed examination of these subclusters, we outlined the features of the excluded altered
297 oocyte cluster. Principal component analysis (PCA) across all oocyte samples revealed a representation of
298 altered oocyte characteristics in PC1, whereas PC2 appeared to represent oocyte growth (Fig S3A).
299 Analysis of developmental oocyte marker expression and flow cytometry-derived cell size data indicated a
300 mixed composition of dormant and activated oocytes within the altered oocyte subcluster (Fig S3B). The
301 significantly low values for total sequence and percent intron, referred to in Fig 2E, suggest transcriptional
302 inactivity in the altered oocytes (Fig S3C). Factor loading in the PCA suggests that these distinct
303 characteristics result from a widespread reduction in gene expression, including *Mdm4*, known for its anti-

304 apoptotic role (Fig S3D and S3E). While our data did not provide insights into the reasons behind the
305 transcription repression, the altered oocytes were presumed to be weakened cells, warranting their exclusion
306 to focus on the transcriptomic changes associated with PFA.

307 DEGs for the Dormant (O1) subcluster encompass *Ankrd36*, whose mutation has been implicated
308 in diminished ovarian reserve [33], as well as *Pm20d1*, which has been noted for its potential involvement
309 in the pathogenesis of polycystic ovary syndrome [34,35] (Fig 5D). DEGs for the Activated-Ctrl (O2)
310 subcluster contain famous oocyte-specific genes typically found in mature oocytes like *Dppa5a*, *Kpna7*,
311 *Khdc3* and *Nlrp4a* [36–39], whereas the Activated-cKO (O3) subcluster showed lower expression of these
312 genes (Fig 5D). Among the 10 DEGs of the Activated-cKO (O3) subcluster, genes such as *Nr1h2*, which
313 has been implicated in lipid metabolism, *Eno1*, linked to glycolysis, and *Adrm1*, a constituent of
314 proteasomes, imply a shift in trophic status (Fig 5D).

315 Due to the limited number of DEGs, GO analysis yielded only a few significant terms (Table S7).
316 Yet, we observed high expression levels of mitochondrial genes and ribosome-related genes in the Dormant
317 (O1) subcluster (Fig 5E), which have been documented in previous studies [40]. Immunostaining verified
318 the expression levels of RPLP1 and RPL27A in DDX4-positive oocytes (Fig 5F). Both RPLP1 and RPL27A
319 showed the highest expression in oocytes smaller than 20 μm, which are presumed to be dormant in
320 primordial follicles (Fig 5G and 5H), while downregulated expression of RPLP1 and RPL27A was noted
321 in oocytes 30-50 μm diameter, which are often observed in secondary follicles. In oocytes smaller than 20
322 μm, *Wls* cKO mice showed a significantly lower intensity of these ribosomal proteins compared to controls,
323 although the difference was not substantial.

324 We then examined DEGs using the singleCellHaystack method to test how GC mis-differentiation
325 in *Wls* cKO ovaries affects the transcriptome of interacting oocytes. That analysis identified 1,132 DEGs
326 that were effectively represented by four expression patterns (clusters 1–4) (Fig 6A and Table S8). We
327 expected that the retained nuclear localization of FOXO3 in growing *Wls* cKO oocytes would result in the
328 constant up-regulation of "dormant" genes even after PFA stimulus. However, we failed to detect a cluster
329 of genes expressed in such a manner (Fig 6B). Instead, the majority of genes (81%) showed similar

330 expression kinetics between control and *Wls* cKO samples with associated expression changes with PFA
331 (Cluster 1: 224 genes up-regulated in dormant oocytes; Clusters 3 and 4: 429 and 281 genes, respectively,
332 up-regulated in activated oocytes) (Fig 6A). Interestingly, Cluster 2 (198 genes) showed a significant down-
333 regulation both in dormant and in activated oocytes in *Wls* cKO mice (Fig 6B). We then explored the
334 functional association of these DEGs using available databases (Gene Ontology, UK Biobank GWAS and
335 MSigDB Oncogenic Signature). Although there were no significantly enriched terms from those databases,
336 there were notable possible WNT-associated terms of "Wnt up-regulation associated oncogenes" (*Btg4*,
337 *Fabp5*, *Myo5b*, *Mtf1*, *Ckap4*) and "age at menopause" (*Ddx17*, *Akap13*, *Slco4a1*) at the top of the term lists,
338 suggesting a possible molecular crosstalk between (pre-)GCs and oocytes related to the cause of infertility
339 via defective WNT-signaling (Table S9). After examining all available TF databases implemented in
340 Enrichr, there was no evidence of enrichment of FOXO3-related terms in any of the DEG clusters, even
341 when the kinetics were classified into 4 to 6 clusters (Fig S4).

342 Finally, we investigated gene regulatory networks during PFA by performing gene co-expression
343 analysis based on the DEGs detected in the Seurat analysis (Fig 6C). We identified hub genes within the
344 top 20, whose expression was well represented before and after activation and by genotype (Fig 6D). *Zfp57*
345 and *Foxr1*, known as oocyte-specific genes, are hub gene candidates that are preferentially expressed in
346 activated oocytes, including the Activated-Ctrl (O2) and Activated-cKO (O3) subclusters (Fig 6D).
347 Consistent with our results, *Foxr1* has been reported to be upregulated after PFA [41], suggesting that these
348 transcription factors are likely activated during PFA regardless of aberrant GC cell activation in *Wls* cKO
349 mice. *Nr1h2* and *Eno1*, while DEGs in the O3 subcluster are hub gene candidates upregulated in oocytes
350 from *Wls* cKO mice (Fig 6D). *Nr1h2* is known to be predominantly expressed in non-growing oocytes,
351 indicating an unbalanced undifferentiated state in *Wls* cKO ovaries [42]. Another hub gene candidate,
352 *Sp110*, is expressed predominantly in the Activated-Ctrl (O2) subgroup and is known to increase after PFA
353 (Fig 6D) [41]. *Sp110* expression might be indirectly regulated by GCs receiving WNT signaling. Altogether,
354 these results depict regulatory features of oocyte gene expression that are affected by the direct and indirect
355 impact of surrounding GCs with or without WNT signaling during PFA.

356

357 # Discussion

358 In this study, we uncover for the first time the single-cell resolution regulatory dynamics of a PFA process
359 using a unique model, *Wls* cKO mice. In *Wls* cKO mice, nearly all GCs, except pre-GCs, have a
360 disorganized phenotype, which results in complete female infertility due to the inability to support oocyte
361 growth. Consistent with that phenotype, the transcriptome landscapes of control and *Wls* cKO cells were
362 similar until the pre-GC stage prior to PFA. The transcriptomic features of *Wls* cKO mice became apparent
363 immediately in GCs after PFA, although the features of *Wls* cKO-derived oocytes were more modest than
364 expected at the transcriptomic level. There was little evidence of the continuous up-regulation of "dormancy
365 genes" in activated oocytes from *Wls* cKO mice, as expected from FOXO3 being retained in the nuclei of
366 growing oocytes. However, the loss of WNT signaling in pre-GCs and GCs affects the oocyte
367 transcriptomes with distinct molecular signatures via a possible molecular crosstalk as well as a poor
368 surrounding environment, which results in infertility. Our data emphasize the impact of WNT signaling on
369 GC identity and GC-oocyte interactions, organizing the transcriptional regulation that is crucial for normal
370 follicular development.

371 In the GC lineage from *Wls* cKO ovaries, some genes were erroneously up-regulated after the
372 initiation of PFA. Particularly, TGFβ/BMP signaling appears to remain active throughout GC
373 subpopulations, marked by the elevated expression of *Bmp2*. TGFβ superfamily members are expressed in
374 various ovarian cell types [43]. While *Bmp2* typically functions in late GCs of antral follicles during late
375 folliculogenesis [44,45], the elevated expression of *Bmp2* in atretic GCs during early folliculogenesis in
376 rats [43] suggests a potential for atretic conditions in GCs of *Wls* cKO mice. A similar abnormal
377 morphology of GCs in *Wls* cKO mice has been reported in GCs under Müllerian inhibiting substance (MIS)-
378 treatment, which suppresses the proliferation and differentiation of mouse GCs [17]. Both MIS signaling
379 and WNT pathways play integral roles in GC proliferation and maturation. Given the identified potential
380 upregulation of TGFβ/BMP signaling both in MIS-treated mice and in *Wls* cKO mice, the precise

381 suppression of TGFβ/BMP signaling may be crucial for the pre-GC to GC transition.

382 Notably, genes associated with protein quality control have a decreased expression in *Wls* cKO
383 GCs, indicating a potential dysfunction of proteostasis. This result supports the potential regulation of
384 protein quality control by WNT signaling, suggesting there is a crucial interplay to achieve cellular
385 homeostasis and function. In addition to that, the observed downregulation of *Fosb* in *Wls* cKO GCs as a
386 potential expression regulator, is reminiscent of its reported decline with age in primate datasets [40]. This
387 suggests intriguing parallels between the molecular profiles of *Wls* cKO GCs and those associated with
388 aging. Unraveling the intricate connections between WNT signaling and the aging process in GCs may
389 provide insights into the age-related decline in ovarian function.

390 In this study, we identified an altered oocyte cluster characterized by a low transcriptional level in
391 *Wls* cKO mice, which allows us to elucidate the impact of GC dysfunction on oocyte conditions. That
392 cluster appeared to encompass both dormant and activated oocytes, suggesting a complex interplay between
393 GC maturation and oocyte state. The present data set does not conclusively elucidate the reason(s) for the
394 division of the oocyte population into two distinct states in *Wls* cKO ovaries. However, based on the
395 presence of the altered oocyte cluster and the terminal phenotype of oocyte depletion in adult *Wls* cKO
396 ovaries [15], we infer that all oocytes will eventually shift to the altered oocyte cluster and undergo atresia.
397 Further clarification of the cellular lineage and the impact of unhealthy GCs may offer valuable insights
398 into the underlying mechanisms governing oocyte integrity and atresia.

399 Activated oocytes in *Wls* cKO mice showed modest transcriptome alterations compared to the
400 control, with parallel expression changes associated with PFA. However, the singleCellHaystack method
401 revealed a notable down-regulation of the set of genes even before PFA initiation in *Wls* cKO mice-derived
402 oocytes, which contrasts with pre-GCs in *Wls* cKO ovaries that appeared normal in the transcriptome as
403 well as our previous histological observations [15]. The enriched tendency of genes known to have a
404 positive regulatory correlation with WNT only in control oocytes suggests that these down-regulated genes
405 are caused by WNT signaling-dependent molecular cross-talk in (pre-)GC-oocyte interactions, rather than
406 being solely influenced by the surrounding microenvironments. This result implies the possibility that

407 oocytes directly receive WNT ligands from (pre-)GCs. Previous reports of the over-activation of WNT
408 signaling in oocytes by the constitutive expression of active β-catenin showed no phenotype in
409 folliculogenesis. It may be that gain-of-function experiments do not adequately reveal the role of WNT
410 signaling in oocyte growth. However, the non-significant term and the detection of only a few DEGs
411 between subclusters support the idea that the absence of the proper microenvironment, which is facilitated
412 by appropriately differentiated GCs, is likely the critical cause of atretic oocytes observed in *Wls* cKO mice
413 at a later stage of folliculogenesis [15].

414 Although the oocytes of *Wls* cKO mice are activated and develop to a certain degree, we previously
415 reported that these growing oocytes partially maintain dormant characteristics, as indicated by the nuclear
416 localization of FOXO3 [15]. In other words, oocyte activation at PFA encompasses two processes: an
417 increase in size and a break from dormancy. *Wls* cKO mice serve as a model where only the growth process
418 occurs. In this study, the PFA process was described as a transcriptomic change. We found that dormancy
419 in oocytes has weak associations with the transcriptional landscape in this context. Nuclear FOXO3 may
420 be insufficient or uncorrelated to the arrest in oocyte size growth and transcriptome activation, key
421 processes in oocyte activation. However, it remains possible that the oocytes we previously observed in
422 *Wls* cKO ovaries belonged to the altered oocyte cluster and that extensive transcriptional downregulation
423 prevented us from detecting transcriptomic changes. WNT-mediated GC function likely facilitates FOXO3
424 nuclear export in oocytes, but Kit signal components, which are upstream of FOXO3 phosphorylation, are
425 unexpectedly up-regulated in *Wls* cKO ovaries [15]. These results suggest a potential compensatory
426 feedback mechanism and/or the importance of an environment such as nutrition and mechanical stress
427 provided by surrounding GCs, emphasizing the need for further experimental studies to fully understand
428 the intricate interactions in this regulatory network.

429 In conclusion, our study on *Wls* cKO ovaries uncovered the intricate impact of WNT signaling on
430 the dynamics of GC differentiation and oocyte activation. WNT signaling may impact reproductive
431 performance through its multifaceted roles in sexual differentiation, follicle development, luteinization and
432 steroid production [46,47]. Upregulated WNT signaling is linked to ovarian cancer in mice and in humans

433 [48,49], and altered WNT-related gene expression has been reported in the ovaries of polycystic ovary
434 syndrome, a potential cause of infertility [50]. Our results contribute to the growing knowledge in this area
435 and may serve as a valuable resource for future investigations into the clinical relevance of WNT signaling.
436 Further studies dissecting the impact of aberrant GCs should provide insights into reproductive biology to
437 address infertility.
438

439 Materials and Methods

440 Animals

441 *Sf1-Cre* mice (stock no. 012462), *Wls*^{flox} mice (stock no. 012888), *Ddx4-Cre* mice (stock no. 006954) and
442 *Ai9* mice (stock no. 007909) were obtained from The Jackson Laboratory [51–54]. *Wls*^{del} mice with a
443 ubiquitous *Wls*^{flox} allele deletion were obtained by crossing *Wls*^{flox} mice with *Ddx4-Cre* mice. Littermate
444 controls, either *Sf1-Cre;Wls*$^{flox/+}$ or *Wls*$^{flox/del}$, were utilized for immunostaining comparisons with *Sf1-*
445 *Cre;Wls*$^{flox/del}$(*Wls* cKO). *Sf1-Cre;Ai9* mice were used to confirm the efficiency of Cre. To prepare single
446 cells for RNA sequencing, *Sf1-Cre;Wls*$^{flox/+}$*;Ai9* mice served as controls for *Sf1-Cre;Wls*$^{flox/del}$*;Ai9* (*Wls*
447 cKO) mice. All animal experiments were approved by the Institutional Animal Care and Use Committee
448 of RIKEN (approval number: A2017-13). All mouse lines were maintained on a mixed genetic background.
449

450 Immunostaining and histology

451 Immunofluorescence staining was performed using ovaries that had been fixed overnight at 4°C with 4%
452 paraformaldehyde in phosphate-buffered saline (PBS). The fixed tissue was dehydrated, embedded in
453 paraffin and then sectioned at a thickness of 5 μm. The sections were depleted of paraffin and rehydrated
454 according to standard protocols. For antigen retrieval, the sections were incubated either at 110°C for 15
455 min with citrate buffer (pH 6.0) or with Tris-EDTA buffer (pH 9.0). After washing with PBS containing
456 0.1% Tween 20 (PBST), the sections were incubated for 1 h at room temperature in a blocking buffer,

457 stained overnight at 4°C with primary antibodies, and then exposed for 2 h at room temperature to a 1:500
458 dilution of appropriate secondary antibodies labeled with Alexa Fluor 488, 568 or 647 (A11057, A21206
459 and A10042, Thermo Fisher Scientific; or 715-545-151, Jackson Immuno Research). The primary
460 antibodies used included mouse anti-DDX4 (1:300; ab27591, Abcam) rabbit anti-DDX4 (1:300; ab13840,
461 Abcam), goat PDLIM4 (1:133; NB100-1382, Novus Biologicals), rabbit anti-IRX3 (1:100, ab242133,
462 Abcam) and rabbit anti-RPLP1 (1:200; NBP1-81293, Novus Biologicals). Antibodies were diluted in
463 blocking buffer or Can Get Signal immunostain solution (NKB-401, Toyobo). DNA was counterstained
464 with 4′,6-diamidino-2-phenylindole (DAPI). Samples were mounted with VECTASHIELD Vibrance
465 Antifade Mounting Medium (H-1700, Vector Laboratories).

466 To assess Cre recombination efficiency, ovaries were fixed overnight at 4°C with 4%
467 paraformaldehyde in PBS. The fixed tissues were immersed in sucrose gradients (10%, 20% and 30%) in
468 PBS sequentially at 4°C; after which the tissues were embedded in an optimal cutting temperature
469 compound. Frozen samples were sectioned at 6 μm using a CryoStar NX70 cryotome (Leica Microsystems).
470 Ovarian cryosections from *Sf1-Cre;Ai9* mice were incubated in blocking buffer for 1 h at room temperature,
471 stained overnight at 4°C with rabbit anti-DDX4 (1:500; ab13840; Abcam) antibody, followed by incubation
472 with donkey anti-rabbit IgG Alexa Fluor 488 (A21206, Thermo Fisher Scientific). DNA was counterstained
473 with DAPI. Samples were mounted using VECTASHIELD Vibrance Antifade Mounting Medium (Vector
474 Laboratories).

475 PAS-H staining was performed according to a standard protocol. In brief, ovaries were fixed in
476 Bouin's solution, embedded in paraffin, and sectioned at a thickness of 5 μm. The sections were hydrated
477 and treated first with a periodic acid solution for 10 min and then with Schiff's reagent for 15 min. Nuclei
478 were counterstained with hematoxylin.

479

480 Ovary dissociation and single-cell sorting

481 At postnatal day (PD) 7, ovaries from euthanized control mice (n=3) and from *Wls* cKO mice (n=8) were

482 collected. Ovaries were treated with a CTK solution (consisting of 0.25% trypsin (Thermo), 0.1%
483 collagenase type IV (Gibco), 20% KSR (Invitrogen) and 1 mM $CaCl_2$ in PBS) for 30 min at 37°C, then
484 further treated with Accutase (Nacalai) at 37°C for 15 min. The reaction was halted by adding L-15 medium
485 with 0.1% penicillin-streptomycin and 5% FBS, and the cells were dissociated by pipetting. The cell
486 suspension was filtered through 70 µm cell strainers, followed by centrifugation at 400 g for 5 min and
487 resuspension in sorting buffer (7.5% BSA (Life Technologies) in PBS). Blocking was performed with rat
488 IgG (5 mg/mL, I8015, Sigma-Aldrich) for 15 min on ice. Subsequently, cell surface staining was conducted
489 using anti-ckit-APC (1:50, 105812, BioLegend) and anti-CD45-Alexa Fluor 488 (1:200, 103122,
490 BioLegend) for 15 min on ice. After centrifugation at 400 g for 5 min, cells were resuspended in sorting
491 buffer. Prior to single-cell sorting by flow cytometry, samples were passed through 40 µm cell strainers,
492 and DAPI (1:10,000) was added. Control and *Wls* cKO samples were each sorted using MoFlo Astrios EQ
493 with Summit v 6.3.0. software (Beckman Coulter) into 384-well plates containing 286 tdTomato-positive
494 somatic cells and 95 ckit-positive oocytes. DAPI-positive dead cells and CD45-positive leukocytes were
495 excluded.
496

497 **RamDA-seq library preparation**

498 Library preparation for RamDA-seq was performed according to a previously report [19]. However, to
499 reduce reagent costs and rRNA-derived sequencing reads, the method was modified as follows: To suppress
500 rRNA-derived cDNA synthesis, 0.008 units/µl XRN-1 (NEB) was added to the genomic DNA digestion
501 mix, and the reaction was performed at 30°C for 5 min. To reduce reagent costs, a liquid dispenser Mantis
502 (Formulatrix) was used to perform the reaction up to second strand synthesis at 1/10 the reaction volume.
503 After that, 2.5 µl 0.8 X Tagment DNA Buffer (Illumina) diluted with RNase-free water was added to 0.5 µl
504 of the second strand synthesis products for dilution. Then, 0.5 µl Amplicon Tagment Mix (Illumina) was
505 added to 1.5 µl of the diluted product, and tagmentation was performed at 55°C for 10 min. After that, the
506 library was prepared using 1/10 the reaction volume according to the Nextera XT DNA Library Prep Kit

507 (Illumina) procedure. Twelve PCR cycles were performed. Somatic and oocyte library products were
508 collected separately in equal volumes of 1 µl/well. Subsequently, 50 µl of each sample was fractionated
509 from the equal mixed library, purified with 1.2X AMPureXP (Beckman Coulter), and eluted with 25 µl TE.
510 To prevent large discrepancies in the number of sequencing reads per cell between somatic and oocyte cells,
511 purified libraries were mixed to ensure a constant average molar per cell type using the quantitative results
512 from the Bioanalyzer Agilent High-Sensitivity DNA Kit and the ratio of the number of cells sorted (somatic
513 cells: oocytes = 286:95). The pooled library of 2.3 pM was sequenced in single end read 76 cycles using
514 NextSeq 500 High Output Kit v2.5.
515

516 **Quality control metrics for RamDA-seq data**

517 The RamDA-seq reads were mapped to the mouse genome (GRCm38) using Hisat2 v2.2.0 [55] after
518 trimming adaptor sequences and low quality bases using Fastq-mcf v1.1.2 in the ea-utils package [56]. The
519 resulting binary alignment/map (BAM) files were sorted using samtools [57] and the final mapping quality
520 was assessed using RSeQC v3.0.1 [58]. The gene count table was obtained using the featureCounts v2.0.1
521 tool in the Subread package [59] with the option '-t exon -g gene_id' and the annotation gtf file from
522 GENCODE (vM25). We evaluated the quality control metrics and filtered out low quality samples based
523 on the RNA integrity assessed by coverage profile along the gene body and the number of detected genes
524 ≤ 8,000. We performed downstream analysis on the remaining data from 350 and 371 cells from control
525 and *Wls* cKO mice, respectively.
526

527 **Sequence data analysis**

528 Seurat v3.2.2 [60] was used for clustering and differential gene expression analysis of scRNA-seq data for
529 control and *Wls* cKO samples independently using the same parameters. The read counts were normalized
530 as log scaled transcripts per million (TPM). Dimensionality reduction and clustering were performed using
531 the 'FindClusters' function of Seurat with the default parameters except for 'resolution = 1', using the top

532 2,000 variable genes. Since our clustering detected a possible altered GC population, the percentage of
533 intron reads and the abundance of nuclear ncRNA, using Malat1 as a marker, were evaluated to assess cell
534 viability. Enrichment of GO (Biological Process) for marker genes of each cluster was tested using Enrichr
535 [61].

536 Detailed subpopulation analyses were performed for each oocyte and GC population after pooling
537 the control and *Wls* cKO datasets. In this analysis, we excluded the altered GC population in *Wls* cKO
538 samples. We used Seurat for clustering and exploration of DEGs with the same settings used for the above
539 whole cell dataset. DEGs, defined as false discovery rate (FDR) < 0.05, were identified using the
540 'FindAllMarkers' function of the Seurat. For the subpopulation analysis, due to the complicated nature of
541 cell clustering relationships, DEGs were further explored using singleCellHaystack v0.3.4, which identifies
542 DEGs without relying on the clustering of cells using the Kullback-Leibler Divergence method [22]. This
543 analysis was performed using the "highD" method with the following options: for GCs, all 40 principal
544 components with grid.points = 30, while for oocytes, top 22 principal components, whose cumulative
545 contribution ratio just exceeds 70%, with grid.points = 10 to increase the detectability of DEGs in fewer
546 numbers of cells. The detected DEGs were then classified into four seemingly parsimonious expression
547 kinetic patterns after testing up to six patterns: for GCs, the top 1,000 confidential DEGs based on the FDR
548 were used. These DEGs were used for the subsequent analysis. Enriched functional features of DEGs were
549 tested with Enricher using available databases (Gene Ontology, UK Biobank GWAS, MSigDB Oncogenic
550 Signature and all TF databases). To identify potentially important transcriptional regulators, regulatory
551 network analysis was performed using the GENIE3 package, a random forest method that calculates the
552 links between each gene and all other genes [23]. We used TPM-scaled read counts of DEGs (oocytes: FDR
553 < 0.05 by Seurat; GCs: top 1,000 DEGs by singleCellHaystack) as input. With the information of known
554 mouse transcription factors [62], only the transcriptional regulator-targets connected with thresholds above
555 0.07 were retained and used for the network analysis. The resulting networks were visualized using
556 CytoScape 3.10 [63].
557

558 ## Image analysis

559 Immunostaining was examined using a slide scanner (Axio Scan.Z1, Zeiss) or a confocal laser scanning
560 microscope (LSM780, Zeiss). All images were taken with Axio Scan.Z1 utilizing the tile scan and
561 automated stitching functions.

562 The thickness of the GC layer was determined as half the difference between the diameters of the
563 follicle, and oocytes were measured in PAS-H–stained ovarian sections using ImageJ software (NIH).
564 Oocytes with visible nuclei were analyzed in a single section per ovary from three ovaries for each genotype
565 at PD7.

566 For the measurement of IRX3 signals in pre-GCs/GCs, ovarian sections were subjected to
567 immunofluorescence staining for IRX3, as well as for the oocyte marker DDX4. Follicle boundaries were
568 delineated based on histology, with the DAPI-positive area serving as the measurement region for (pre-)GC
569 analysis. The fluorescence intensity of IRX3 in each region was measured using ImageJ software. More
570 than four ovaries for each genotype, as well as more than one section per ovary, were analyzed.

571 For the quantification of RPLP1 or RPL27A intensities, images of ovarian sections immunostained
572 for RPLP1 or RPL27A were analyzed using ImageJ software in each oocyte area. The regions of the oocyte
573 were determined manually utilizing ImageJ. Oocytes with visible nuclei were analyzed in a single section
574 per ovary from three ovaries for the control group or from four ovaries for the *Wls* cKO group.

575

576 ## Statistical analysis

577 All statistical analyses were performed using GraphPad Prism 9 software. Tests included the nonparametric
578 Mann-Whitney matched-pairs test, unpaired multiple t-tests with the Holm-Sidak correction, two-way
579 analysis of variance (ANOVA) with Sidak's post-hoc test for multiple comparisons, and a chi-square test
580 for trend for the contingency table. Regression lines were fitted with the scatterplot of GC thickness data
581 for control and for *Wls* cKO mice, and then analysis of covariance (ANCOVA) analysis was performed. A
582 P value of <0.05 was considered statistically significant.

583

584 # Acknowledgments

585 We thank A. Matsushima (RIKEN BDR) for assistance with the infrastructure for the data analysis. This
586 research was supported by the Medical Research Center Initiative for High Depth Omics, Nanken-Kyoten,
587 and Single-cell Omics Laboratory in TMDU.

588

589 # References

590 1. Pepling ME, Spradling AC. Mouse ovarian germ cell cysts undergo programmed breakdown to form
591 primordial follicles. Developmental Biology. 2001; 234:339–351. doi:10.1006/dbio.2001.0269
592 2. Grive KJ, Freiman RN. The developmental origins of the mammalian ovarian reserve. Development.
593 2015; 142:2554–2563. doi:10.1242/dev.125211
594 3. McLaughlin EA, McIver SC. Awakening the oocyte: Controlling primordial follicle development.
595 Reproduction. 2009; 137:1–11. doi:10.1530/REP-08-0118
596 4. Zhang T, He M, Zhang J, Tong Y, Chen T, Wang C, Pan W, Xiao Z. Mechanisms of primordial
597 follicle activation and new pregnancy opportunity for premature ovarian failure patients. Front
598 Physiol. 2023;14:1113684. doi: 10.3389/fphys.2023.1113684
599 5. Reddy P, Liu L, Adhikari D, Jagarlamudi K, Rajareddy S, Shen Y, et al. Oocyte-specific deletion
600 of pten causes premature activation of the primordial follicle pool. Science. 2008; 319: 611–613.
601 doi:10.1126/science.1152257
602 6. Castrillon DH, Miao L, Kollipara R, Horner JW, DePinho RA. Suppression of ovarian follicle
603 activation in mice by the transcription factor Foxo3a. Science. 2003; 301:215–218.
604 doi:10.1126/science.1086336
605 7. Ford EA, Beckett EL, Roman SD, McLaughlin EA, Sutherland JM. Advances in human primordial
606 follicle activation and premature ovarian insufficiency. Reproduction. 2020; 159:R15-R29.

607 doi:10.1530/REP-19-0201

608 8. Pelosi E, Omari S, Michel M, Ding J, Amano T, Forabosco A, et al. Constitutively active Foxo3 in
609 oocytes preserves ovarian reserve in mice. Nature Communications. 2013; 4:1843.
610 doi:10.1038/ncomms2861

611 9. John GB, Gallardo TD, Shirley LJ, Castrillon DH. Foxo3 is a PI3K-dependent molecular switch
612 controlling the initiation of oocyte growth. Developmental Biology. 2008; 321: 197–204.
613 doi:10.1016/j.ydbio.2008.06.017

614 10. Dong J, Albertini DF, Nishimori K, Kumar TR, Lu N, Matzuk MM. Growth differentiation factor-
615 9 is required during early ovarian folliculogenesis. Nature. 1996; 383:531–535.
616 doi:10.1038/383531a0

617 11. Zhang H, Risal S, Gorre N, Busayavalasa K, Li X, Shen Y, Bosbach B, Brännström M, Liu K.
618 Somatic cells initiate primordial follicle activation and govern the development of dormant oocytes
619 in mice. Current Biology. 2014; 24:2501–8. doi:10.1016/j.cub.2014.09.023

620 12. Shimamoto S, Nishimura Y, Nagamatsu G, Hamada N, Kita H, Hikabe O, et al. Hypoxia induces
621 the dormant state in oocytes through expression of Foxo3. The Proceedings of the National
622 Academy of Sciences. 2019; 116:12321-12326. doi:10.1073/pnas.1817223116

623 13. Nagamatsu G, Shimamoto S, Hamazaki N, Nishimura Y, Hayashi K. Mechanical stress
624 accompanied with nuclear rotation is involved in the dormant state of mouse oocytes. Science
625 Advances. 2019; 5:eaav. doi:10.1126/SCIADV.AAV9960

626 14. De Cian MC, Gregoire EP, Le Rolle M, Lachambre S, Mondin M, Bell S, et al. R-spondin2 signaling
627 is required for oocyte-driven intercellular communication and follicular growth. Cell Death &
628 Differentiation. 2020; 27:2856–2871. doi:10.1038/s41418-020-0547-7

629 15. Habara O, Logan CY, Kanai-Azuma M, Nusse R, Takase HM. WNT signaling in pre-granulosa
630 cells is required for ovarian folliculogenesis and female fertility. Development. 2021;
631 148:dev198846. doi:10.1242/dev.198846

632 16. Suzuki H, Kanai-Azuma M, Kanai Y. From Sex Determination to Initial Folliculogenesis in

633 Mammalian Ovaries: Morphogenetic Waves along the Anteroposterior and Dorsoventral Axes.
634 Sexual Development. 2015; 9:190–204. doi:10.1159/000440689
635 17. Meinsohn MC, Saatcioglu HD, Wei L, Li Y, Horn H, Chauvin M, et al. Single-cell sequencing
636 reveals suppressive transcriptional programs regulated by MIS/AMH in neonatal ovaries. The
637 Proceedings of the National Academy of Sciences. 2021; 118:e2100920118.
638 doi:10.1073/PNAS.2100920118
639 18. Umeno K, Sasaki A, Kimura N. The impact of oocyte death on mouse primordial follicle formation
640 and ovarian reserve. Reproductive Medicine and Biology. 2022; 21:e12489.
641 doi:10.1002/RMB2.12489
642 19. Hayashi T, Ozaki H, Sasagawa Y, Umeda M, Danno H, Nikaido I. Single-cell full-length total RNA
643 sequencing uncovers dynamics of recursive splicing and enhancer RNAs. Nature Communications.
644 2018; 9:619. doi:10.1038/S41467-018-02866-0
645 20. Granados-Aparici S, Hardy K, Franks S, Sharum IB, Waite SL, Fenwick MA. SMAD3 directly
646 regulates cell cycle genes to maintain arrest in granulosa cells of mouse primordial follicles.
647 Scientific Reports. 2019; 9:6513. doi:10.1038/s41598-019-42878-4
648 21. Morris ME, Meinsohn MC, Chauvin M, Saatcioglu HD, Kashiwagi A, Sicher NA, et al. A single-
649 cell atlas of the cycling murine ovary. Elife. 2022;11:e77239. doi:10.7554/eLife.77239
650 22. Vandenbon A, Diez D. A clustering-independent method for finding differentially expressed genes
651 in single-cell transcriptome data. Nature Communications. 2020; 11:4318. doi:10.1038/s41467-
652 020-17900-3
653 23. Huynh-Thu VA, Irrthum A, Wehenkel L, Geurts P. Inferring regulatory networks from expression
654 data using tree-based methods. PLoS One. 2010; 5:e12776.
655 doi:10.1371/JOURNAL.PONE.0012776
656 24. Duggavathi R, Volle DH, Mataki C, Antal MC, Messaddeq N, Auwerx J, et al. Liver receptor
657 homolog 1 is essential for ovulation. Genes & Development. 2008; 22:1871–1876.
658 doi:10.1101/GAD.472008

659 25. Fan HY, O'Connor A, Shitanaka M, Shimada M, Liu Z, Richards JS. β-Catenin (CTNNB1)
660 promotes preovulatory follicular development but represses LH-mediated ovulation and
661 luteinization. Molecular Endocrinology. 2010; 24:1529–1542. doi:10.1210/me.2010-0141
662 26. Kajitani T, Mizutani T, Yamada K, Yazawa T, Sekiguchi T, Yoshino M, et al. Cloning and
663 characterization of granulosa cell high-mobility group (HMG)-box protein-1, a novel HMG-box
664 transcriptional regulator strongly expressed in rat ovarian granulosa cells. Endocrinology. 2004;
665 145: 2307–2318. doi:10.1210/EN.2003-1343
666 27. Cao P, Yang W, Wang P, Li X, Nashun B. Characterization of DNA Methylation and Screening of
667 Epigenetic Markers in Polycystic Ovary Syndrome. Frontiers in Cell and Developmental Biology.
668 2021; 9:664843. doi:10.3389/fcell.2021.664843
669 28. Song J, Diao F, Ma X, Xu S, Cui Y, Jiang S, et al. Androgen upregulates NR4A1 via the TFAP2A
670 and ETS signaling networks. The International Journal of Biochemistry & Cell Biology. 2019;
671 113:1–7. doi:10.1016/J.BIOCEL.2019.05.015
672 29. Fu A, Koth ML, Brown RM, Shaw SA, Wang L, Krentz KJ, et al. IRX3 and IRX5 collaborate during
673 ovary development and follicle formation to establish responsive granulosa cells in the adult mouse.
674 Biology of Reproduction. 2020; 103:620–629. doi:10.1093/BIOLRE/IOAA100
675 30. Hughes CHK, Smith OE, Meinsohn MC, Brunelle M, Gévry N, Murphy BD. Steroidogenic factor
676 1 (SF-1; Nr5a1) regulates the formation of the ovarian reserve. P The Proceedings of the National
677 Academy of Sciences. 2023; 120:e2220849120. doi: 10.1073/pnas.2220849120
678 31. Sharma SC, Richards JS. Regulation of AP1 (Jun/Fos) factor expression and activation in ovarian
679 granulosa cells. Relation of JunD and Fra2 to terminal differentiation. Journal of Biological
680 Chemistry. 2000; 275:33718–33728. doi:10.1074/jbc.M003555200
681 32. Wigglesworth K, Lee KB, Emori C, Sugiura K, Eppig JJ. Transcriptomic diversification of
682 developing cumulus and mural granulosa cells in mouse ovarian follicles. Biology of Reproduction.
683 2015; 92:23. doi:10.1095/biolreprod.114.121756
684 33. Li N, Xu W, Liu H, Zhou R, Zou S, Wang S, et al. Whole exome sequencing reveals novel variants

685 associated with diminished ovarian reserve in young women. Frontiers in Genetics. 2023;
686 14:1154067. doi:10.3389/fgene.2023.1154067
687 34. Li M, Gao S, Kang M, Zhang X, Lan P, Wu X et al. Quercitrin alleviates lipid metabolism disorder
688 in polycystic ovary syndrome-insulin resistance by upregulating PM20D1 in the PI3K/Akt pathway.
689 Phytomedicine. 2023; 117:154908. doi:10.1016/j.phymed.2023.154908
690 35. Sun Q, Gao Y, Yang J, Lu J, Feng W, Yang W. Mendelian Randomization Analysis Identified
691 Potential Genes Pleiotropically Associated with Polycystic Ovary Syndrome. Reproductive
692 Sciences. 2022; 29:1028–1037. doi:10.1007/s43032-021-00776-z
693 36. Pierre A, Gautier M, Callebaut I, Bontoux M, Jeanpierre E, Pontarotti P, et al. Atypical structure
694 and phylogenomic evolution of the new eutherian oocyte- and embryo-expressed
695 KHDC1/DPPA5/ECAT1/OOEP gene family. Genomics. 2007; 90:583–594.
696 doi:10.1016/J.YGENO.2007.06.003
697 37. Hu J, Wang F, Yuan Y, Zhu X, Wang Y, Zhang Y, et al. Novel Importin-α Family Member Kpna7
698 Is Required for Normal Fertility and Fecundity in the Mouse. Journal of Biological Chemistry. 2010;
699 285: 33113–33122. doi:10.1074/JBC.M110.117044
700 38. Ohsugi M, Zheng P, Baibakov B, Li L, Dean J. Maternally derived FILIA-MATER complex
701 localizes asymmetrically in cleavage-stage mouse embryos. Development. 2008; 135:259–69.
702 doi:10.1242/dev.011445
703 39. Tian X, Pascal G, Monget P. Evolution and functional divergence of NLRP genes in mammalian
704 reproductive systems. BMC Ecology and Evolution. 2009; 9:202. doi:10.1186/1471-2148-9-202
705 40. Wang S, Zheng Y, Li J, Yu Y, Zhang W, Song M, et al. Single-Cell Transcriptomic Atlas of Primate
706 Ovarian Aging. Cell. 2020; 180:585–600.e19. doi:10.1016/j.cell.2020.01.009
707 41. Hamazaki N, Kyogoku H, Araki H, Miura F, Horikawa C, Hamada N, et al. Reconstitution of the
708 oocyte transcriptional network with transcription factors. Nature. 2021; 589:264–269.
709 doi:10.1038/s41586-020-3027-9
710 42. Gu C, Liu S, Wu Q, Zhang L, Guo F. Integrative single-cell analysis of transcriptome, DNA

711 methylome and chromatin accessibility in mouse oocytes. Cell Research. 2019; 29:110–123.
712 doi:10.1038/s41422-018-0125-4
713 43. Erickson GF, Shimasaki S. The spatiotemporal expression pattern of the bone morphogenetic
714 protein family in rat ovary cell types during the estrous cycle. Reproductive Biology and
715 Endocrinology. 2003; 1:9. doi:10.1186/1477-7827-1-9
716 44. Inagaki K, Otsuka F, Miyoshi T, Yamashita M, Takahashi M, Goto J, et al. p38-Mitogen-Activated
717 Protein Kinase Stimulated Steroidogenesis in Granulosa Cell-Oocyte Cocultures: Role of Bone
718 Morphogenetic Proteins 2 and 4. Endocrinology. 2009; 150:1921–1930. doi:10.1210/EN.2008-0851
719 45. Wu YT, Chang HM, Huang HF, Sheng JZ, Leung PC. Bone morphogenetic protein 2 regulates cell–
720 cell communication by down-regulating connexin43 expression in luteinized human granulosa cells.
721 Molecular Human Reproduction. 2017; 23:155–165. doi:10.1093/MOLEHR/GAW078
722 46. Hernandez Gifford JA. The role of WNT signaling in adult ovarian folliculogenesis. Reproduction.
723 2015; 150:R137–148. doi:10.1530/REP-14-0685
724 47. Boyer A, Lapointe É, Zheng X, Cowan RG, Li H, Quirk SM, et al. WNT4 is required for normal
725 ovarian follicle development and female fertility. The FASEB Journal. 2010; 24:3010–3025.
726 doi:10.1096/fj.09-145789
727 48. Boerboom D, Paquet M, Hsieh M, Liu J, Jamin SP, Behringer RR, et al. Misregulated Wnt/β-catenin
728 signaling to ovarian granulosa cell tumor development. Cancer Research. 2005; 65:9206–9215.
729 doi:10.1158/0008-5472.CAN-05-1024
730 49. Arend RC, Londoño-Joshi AI, Straughn JM, Buchsbaum DJ. The Wnt/β-catenin pathway in ovarian
731 cancer: a review. Gynecologic Oncology. 2013; 131:772–779. doi:10.1016/J.YGYNO.2013.09.034
732 50. Jansen E, Laven JSE, Dommerholt HBR, Polman J, Van Rijt C, Van Den Hurk C, et al. Abnormal
733 gene expression profiles in human ovaries from polycystic ovary syndrome patients. Molecular
734 Endocrinology. 2004; 18:3050–3063. doi:10.1210/me.2004-0074
735 51. Carpenter AC, Rao S, Wells JM, Campbell K, Lang RA. Generation of mice with a conditional null
736 allele for Wntless. Genesis. 2010; 48:554–558. doi:10.1002/dvg.20651

737 52. Dhillon H, Zigman JM, Ye C, Lee CE, McGovern RA, Tang V, et al. Leptin directly activates SF1
738 neurons in the VMH, and this action by leptin is required for normal body-weight homeostasis.
739 Neuron. 2006; 49:191–203. doi:10.1016/j.neuron.2005.12.021
740 53. Madisen L, Zwingman TA, Sunkin SM, Oh SW, Zariwala HA, Gu H, et al. A robust and high-
741 throughput Cre reporting and characterization system for the whole mouse brain. Nature
742 Neuroscience. 2010; 13:133–140. doi:10.1038/nn.2467
743 54. Zhou B, Ma Q, Rajagopal S, Wu SM, Domian I, Rivera-Feliciano J, et al. Epicardial progenitors
744 contribute to the cardiomyocyte lineage in the developing heart. Nature. 2008; 454:109–113.
745 doi:10.1038/nature07060
746 55. Kim D, Paggi JM, Park C, Bennett C, Salzberg SL. Graph-based genome alignment and genotyping
747 with HISAT2 and HISAT-genotype. Nat Biotechnol. 2019; 37:907–915. doi:10.1038/s41587-019-
748 0201-4
749 56. Aronesty E. ea-utils : Command-line tools for processing biological sequencing data. 2011.
750 https://expressionanalysis.github.io/ea-utils/.
751 57. Danecek P, Bonfield JK, Liddle J, Marshall J, Ohan V, Pollard MO, et al. Twelve years of SAMtools
752 and BCFtools. Gigascience. 2021; 10:giab008. doi:10.1093/gigascience/giab008
753 58. Wang L, Wang S, Li W. RSeQC: Quality control of RNA-seq experiments. Bioinformatics. 2012;
754 28:2184–2185. doi:10.1093/bioinformatics/bts356
755 59. Liao Y, Smyth GK, Shi W. FeatureCounts: An efficient general purpose program for assigning
756 sequence reads to genomic features. Bioinformatics. 2014; 30:923–930.
757 doi:10.1093/bioinformatics/btt656
758 60. Stuart T, Butler A, Hoffman P, Hafemeister C, Papalexi E, Mauck WM, et al. Comprehensive
759 Integration of Single-Cell Data. Cell. 2019; 177:1888–1902.e21. doi:10.1016/j.cell.2019.05.031
760 61. Xie Z, Bailey A, Kuleshov M V., Clarke DJB, Evangelista JE, Jenkins SL, et al. Gene Set
761 Knowledge Discovery with Enrichr. Current Protocols. 2021; 1:e90. doi:10.1002/cpz1.90
762 62. Alam T, Agrawal S, Severin J, Young RS, Andersson R, Arner E, et al. Comparative transcriptomics

763 of primary cells in vertebrates. Genome Research. 2020; 30:951–961. doi:10.1101/gr.255679.119

764 63. Shannon P, Markiel A, Ozier O, Baliga NS, Wang JT, Ramage D, et al. Cytoscape: A software

765 Environment for integrated models of biomolecular interaction networks. Genome Research. 2003;

766 13:2498–2504. doi:10.1101/gr.1239303

767 # Figure Legends

768

769 **Fig 1. Suppressed WNT signaling in pre-GCs leads to insufficient differentiation of the GC layer in**
770 **growing follicles.** (**A**) Immunofluorescence staining of DDX4 (magenta) in the ovaries of *Wls* cKO mice
771 and littermate control mice at PD7. Nuclei were counterstained with DAPI (cyan). White dotted lines
772 indicate follicles. Scale bars, 200 μm (leftmost panels) or 20 μm (other panels). (**B**) Scatter plot for the
773 distribution of oocyte diameter and GC layer thickness for follicles of *Wls* cKO (n=161 follicles) and control
774 (n=241 follicles) mice at PD7. Solid lines represent the linear regression fit with equations. (**C**)
775 Immunofluorescence staining of DDX4 (green) and tdTomato fluorescence (magenta) in the ovaries of 2-
776 week-old *Sf1-Cre;Ai9* mice. (**D**) Experimental design for scRNA-seq analysis. Ovaries from *Wls* cKO (cKO,
777 *Sf1-Cre;Wls*$^{flox/del}$*;Ai9*, n=8) or littermate control (Ctrl, *Sf1-Cre;Wls*$^{flox/+}$*;Ai9*, n=3) mice were collected at
778 PD7 after which single-cell suspensions were obtained. scRNA-seq was performed using RamDA-seq and
779 the data were then analyzed.

780

781 **Fig 2. scRNA-seq of PD7 ovaries reveals a cellular signature derived from *Wls* cKO mouse ovaries.**
782 (**A, B**) Uniform manifold approximation and projection (UMAP) plots of unbiased clustering of ovarian
783 cells from control mice (**A**, *Sf1-Cre;Wls*$^{flox/+}$*;Ai9*, n=350 cells) or from *Wls* cKO mice (**B**, *Sf1-*
784 *Cre;Wls*$^{flox/del}$*;Ai9*, n=371 cells), where each dot represents an individual cell that is color-coded based on
785 its identified clusters. (**C, D**) Heatmap of the top 20 DEGs of each cluster for control (**C**) or *Wls* cKO (**D**)
786 samples. The value for each gene is the row-scaled Z-score. Representative DEGs for each cell type are
787 listed on the left. (**E**) UMAP plots showing the expression levels of selected marker genes (*Ddx4*, *Amh*,
788 *Smad3*, *Krt19*, *Col1a1*, *Enpep* and *Pdlim4*) or the ratio of intronic reads (*per_intron*). The color scale
789 represents the gene expression level scaled by the Z-score.

790

791 **Fig 3. Integrated subpopulation analysis identifies distinct subgroups in GC lineages.** (**A**) UMAP plot

792 of GCs color-coded by genotype (Ctrl, blue; *Wls* cKO, red). (**B**) UMAP plot showing the different cell
793 subclusters belonging to the GC lineage. (**C**) Heatmap of the top 20 DEGs of each subcluster. (**D, E**) Dot
794 plots showing the expression of selected markers for subclusters or characteristic features. The dot size
795 represents the ratio of cells expressing a specific marker (TPM > 1), while the color indicates the expression
796 level scaled by the Z-score. (**F**) Representative significantly enriched GO terms for DEGs of the GC
797 subcluster. (**G**) Immunofluorescence staining of PDLIM4 (magenta) and DDX4 (green) in the ovaries of 3-
798 week-old *Wls* cKO mice and littermate control mice. Nuclei were counterstained with DAPI (blue). White
799 dotted lines indicate follicles. Scale bars, 20 μm.
800
801 **Fig 4. Similarities and differences in gene regulatory dynamics in GC activation between control and**
802 ***Wls* cKO mice.** (**A**) UMAP plot showing the average expression level of the genes in each cluster defined
803 by hierarchical clustering (cutting into $k = 4$) of DEGs identified by the singleCellHaystack method. (**B**)
804 Representative enriched GO terms of the clusters. (**C**) Regulatory networks visualizing potential key
805 transcriptional regulators involved in GC differentiation. The top 10 nodes are colored dark blue. (**D**)
806 UMAP plots showing expression levels of selected potential hub genes (*Nr5a2*, *Tcf7*, *Tox2*, *Fosb*, *Ets1*,
807 *Irx3*, *Tsc22d1* and *Bmp2*). The color scale represents the gene expression level scaled by the Z-score. (**E**)
808 Immunofluorescence staining of IRX3 (magenta) and DDX4 (green) in the ovaries of 3-week-old *Wls* cKO
809 mice and littermate control mice. Nuclei were counterstained with DAPI (blue). White dotted lines indicate
810 follicles. Scale bars, 20 μm. (**F**) Violin plots showing fluorescence intensity of IRX3 in (pre-)GCs
811 determined from images similar to those in (E). Horizontal lines represent the median. Statistical
812 comparison was performed by two-way ANOVA with Sidak's multiple comparisons test; ns denotes not
813 significant. Pm, primordial; Pr, primary; Sec, secondary follicles. Sample numbers are indicated in
814 parentheses.
815
816 **Fig 5. Distinct gene expression patterns in dormant and in activated oocytes under the influence of**
817 **insufficient GC maturation.** (**A**) UMAP plot of oocytes color-coded by genotype (Ctrl, blue; *Wls* cKO,

818 red). (**B**) UMAP plot showing the different cell subclusters of oocytes. (**C**) Heatmap of the top 20 DEGs of
819 each subcluster; for the activated-cKO subcluster, all 10 DEGs were used. (**D, E**) Dot plots showing the
820 expression of selected markers for subclusters or characteristic features. The dot size represents the ratio of
821 cells expressing a specific marker (TPM > 1), while the color indicates the average gene expression level
822 scaled by the Z-score. (**F**) Immunofluorescence staining of RPLP1 (magenta) and DDX4 (green) in the
823 ovaries of 3-week-old *Wls* cKO mice and littermate control mice. Nuclei were counterstained with DAPI
824 (blue). White dotted lines indicate follicles. Scale bars, 20 μm. (**G, H**) Boxplots depicting fluorescence
825 intensity of RPLP1 (G) or RPL27A (H) in oocytes determined from immunofluorescent images. Sample
826 numbers are indicated in parentheses. Statistical comparison was performed by two-way ANOVA with
827 Sidak's multiple comparisons test; ns denotes not significant.
828
829 **Fig 6. Analysis of possible molecular crosstalk and regulatory features in the absence of WNT**
830 **signaling.** (**A**) UMAP plots depict the average expression level of DEGs in each cluster defined by
831 hierarchical clustering (cutting into $k = 4$) identified by the singleCellHaystack method. (**B**) Violin plots
832 indicating the expression of DEGs for each cluster within oocyte subclusters (O1–O3) from control and
833 from *Wls* cKO samples. Dmt, Dormant. Act, activated. (**C**) Regulatory networks visualizing potential key
834 transcriptional regulators in oocyte activation. The top 10 nodes are colored dark green, nodes ranked 11-
835 20 are colored green, and the others are colored light green. (**D**) UMAP plots showing expression levels of
836 selected potential hub genes (*Zfp57*, *Foxr1*, *Nr1h2*, *Eno1* and *Sp110*). The color scale represents the gene
837 expression level scaled by the Z-score.
838

Supporting Information

Fig S1. Optical detection of cells and quality control for single-cell RNA sequencing. UMAP plots showing tdTomato-expressing somatic cells (**A**), the KIT-APC positive oocyte population (**B**), the total number of mapped reads (total seq) (**C**), and the number of detected genes (number of genes) (**D**). The color scale represents the gene expression level scaled by the Z-score.

Fig S2. DEG clustering dendrogram of GC populations based on expression kinetics. Diagram of hierarchical clustering based on the kinetics of DEGs obtained by the singleCellHaystack method in the GC population. Color bars represent the clustering result when the dendrogram is cut into 4-6 clusters. The number to the left of each bar indicates the number of clusters. The average expression levels of the genes in each cluster were projected onto UMAP plots below the corresponding bars. More clusters lead to a greater subdivision of the main DEG cluster.

Fig S3. Characteristic features of the altered-oocyte subcluster. (**A**) PCA plots of oocytes. Different colors correspond to subclusters of oocytes. The principal components on the axes capture the major sources of gene expression variation, with their respective contributions indicated in the axis labels. (**B**) Dot plot showing the expression of growing oocyte markers. The dot size represents the ratio of cells expressing a specific marker (TPM > 1), while the color indicates the average gene expression level scaled by the Z-score. (**C**) UMAP plots showing cell size, the total number of mapped reads (total sequence), the ratio of intronic reads (percent intron), the PC1 positive factor loading and the PC1 negative factor loading. (**D**) UMAP plots showing the top 6 characterized genes of PC1 positive factor loading. (**E**) UMAP plots showing the top 6 characterized genes of PC1 negative factor loading.

Fig S4. DEG clustering dendrogram of oocyte populations based on expression kinetics similarity.

864 Diagram of hierarchical clustering based on the kinetics of DEGs obtained by the singleCellHaystack
865 method in the oocyte population. Color bars represent the clustering result when the dendrogram is cut into
866 4-6 clusters. The number on the left of each bar indicates the number of clusters. The average expression
867 level of the genes in each cluster were projected onto UMAP plots below the corresponding bars.
868
869 **Table S1. List of top 20 DEGs for each cluster identified from the PD7 control ovary dataset.**
870
871 **Table S2. List of top 20 DEGs for each cluster identified from the PD7 Wls cKO ovary dataset.**
872
873 **Table S3. List of DEGs identified with Seurat from granulosa cell subpopulation dataset.**
874
875 **Table S4. List of DEGs identified with the singleCellHayStack from the granulosa cell subpopulation**
876 **dataset.**
877
878 **Table S5. List of significantly enriched GOs for cluster (K=4) of DEGs identified by the**
879 **singlecellHayStack from the granulosa cell subpopulation dataset.**
880
881 **Table S6. List of DEGs identified with Seurat from oocyte subpopulation dataset.**
882
883 **Table S7. List of enriched GOs based on DEGs identified with Seurat from oocyte subpopulation**
884 **dataset.**
885
886 **Table S8. List of DEGs identified with the singleCellHayStack from the oocyte subpopulation dataset.**
887
888 **Table S9. Disease database showing ovarian or WNT related defeacts were at top of the erichment**
889 **table. Top 10 terms were listed for the two databases.**

Figure 1

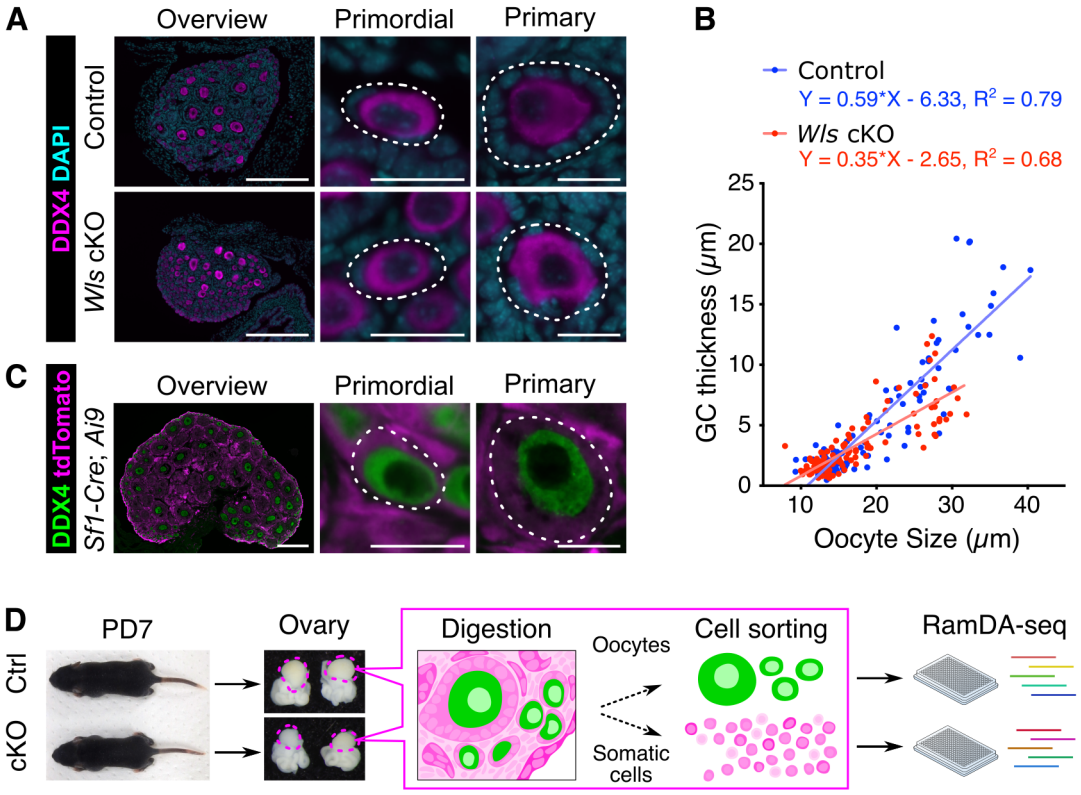
A
Overview
Primordial
Primary
DDX4 DAPI
Control
Wls cKO
B
Control
Y = 0.59*X - 6.33, R2 = 0.79
Wls cKO
Y = 0.35*X - 2.65, R2 = 0.68
GC thickness (μm)
Oocyte Size (μm)
C
DDX4 tdTomato
Sf1-Cre; Ai9
D
PD7
Ctrl
cKO
Ovary
Digestion
Oocytes
Somatic cells
Cell sorting
RamDA-seq

Figure 2

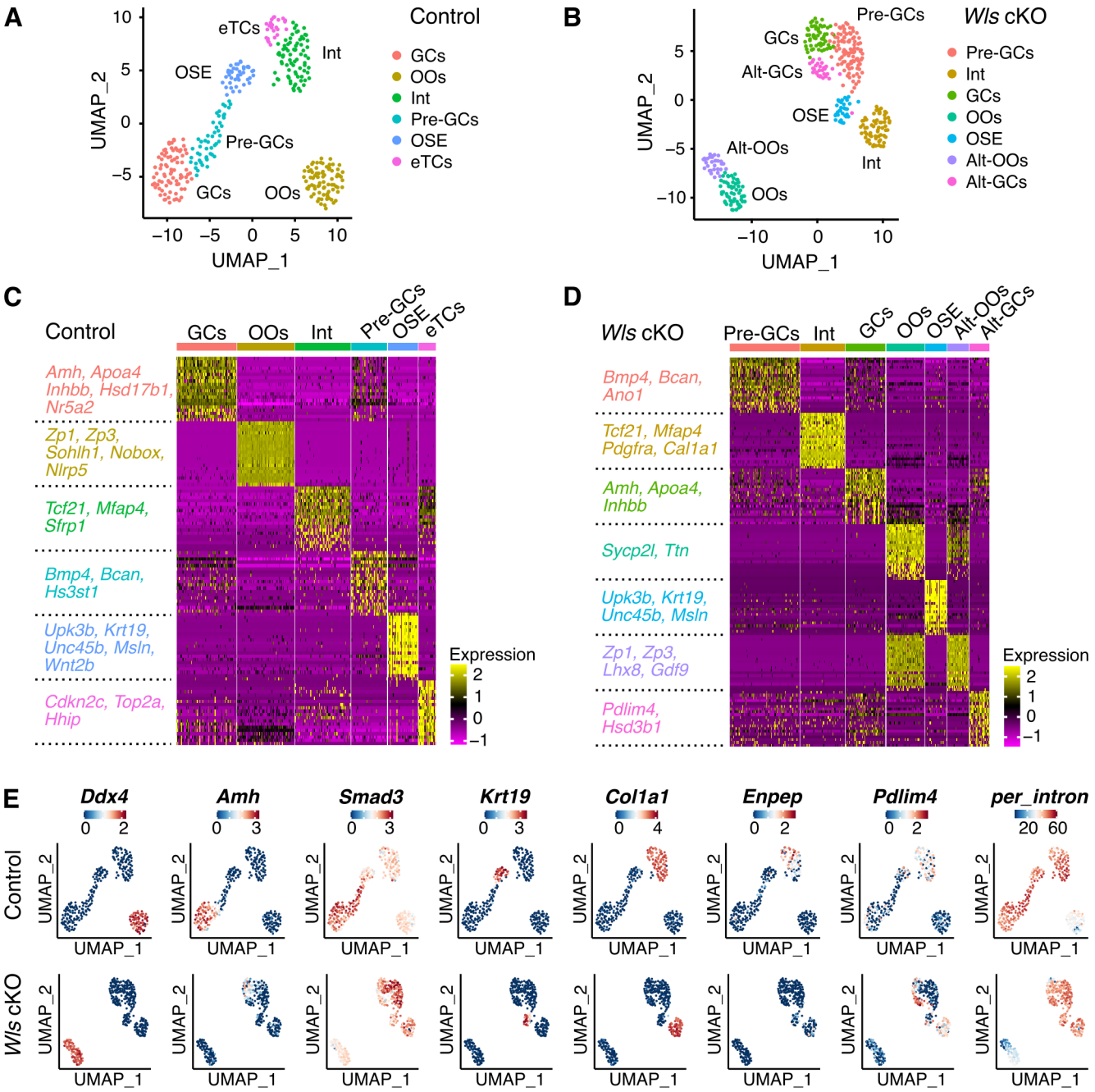
A
Control
eTCs
Int
OSE
Pre-GCs
GCs
OOs
UMAP_2
UMAP_1
GCs
OOs
Int
Pre-GCs
OSE
eTCs
B
Wls cKO
Pre-GCs
GCs
Alt-GCs
OSE
Int
Alt-OOs
OOs
Pre-GCs
Int
GCs
OOs
OSE
Alt-OOs
Alt-GCs
C
Control
GCs
OOs
Int
Pre-GCs
OSE
eTCs
Amh, Apoa4 Inhbb, Hsd17b1, Nr5a2
Zp1, Zp3, Sohlh1, Nobox, Nlrp5
Tcf21, Mfap4, Sfrp1
Bmp4, Bcan, Hs3st1
Upk3b, Krt19, Unc45b, Msln, Wnt2b
Cdkn2c, Top2a, Hhip
Expression
D
Wls cKO
Pre-GCs
Int
GCs
OOs
OSE
Alt-OOs
Alt-GCs
Bmp4, Bcan, Ano1
Tcf21, Mfap4 Pdgfra, Cal1a1
Amh, Apoa4, Inhbb
Sycp2l, Ttn
Upk3b, Krt19, Unc45b, Msln
Zp1, Zp3, Lhx8, Gdf9
Pdlim4, Hsd3b1
Expression
E
Ddx4
Amh
Smad3
Krt19
Col1a1
Enpep
Pdlim4
per_intron
Control
Wls cKO
UMAP_2
UMAP_1

Figure 3

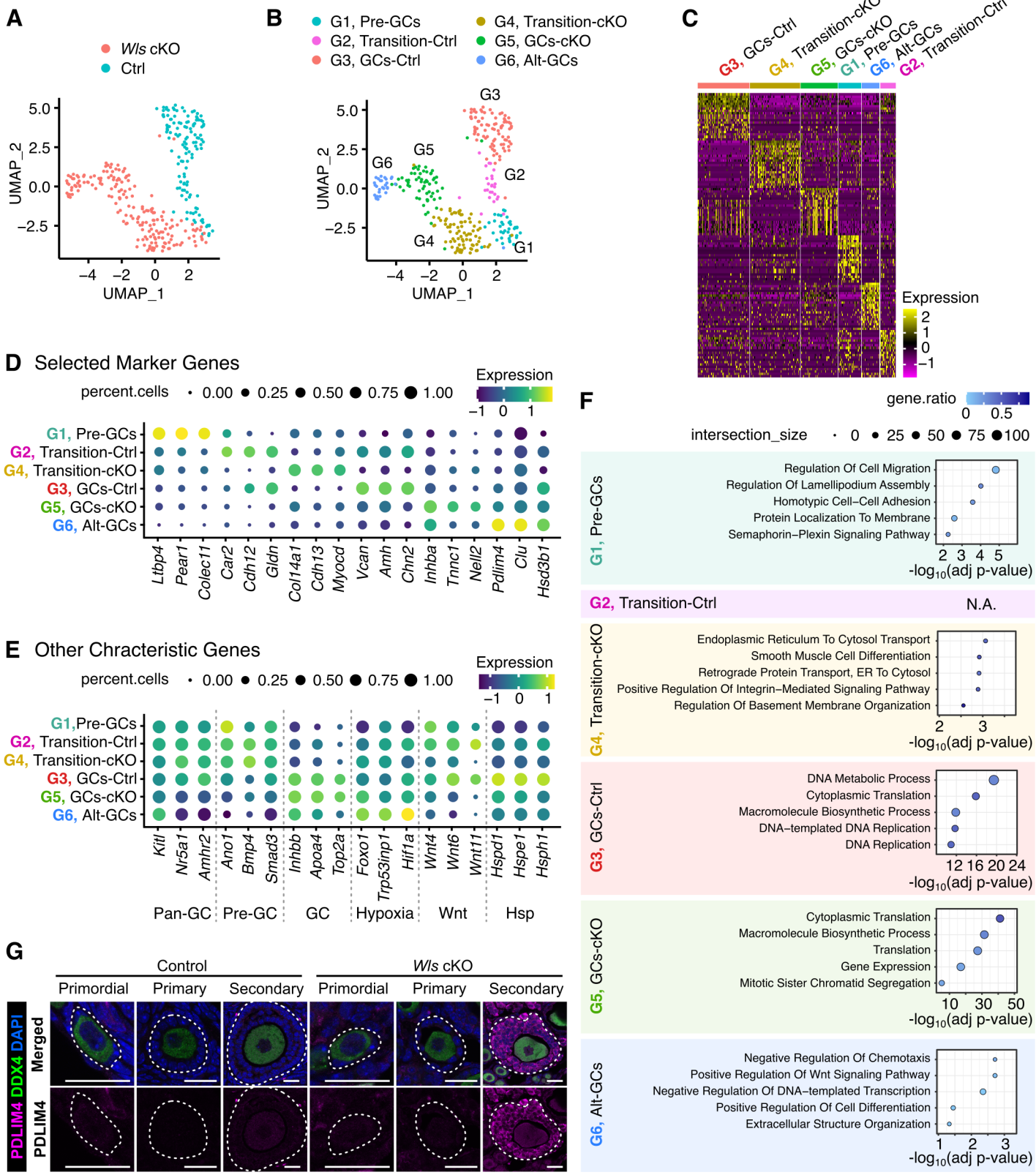
A
Wls cKO
Ctrl
UMAP_2
UMAP_1
B
G1, Pre-GCs
G2, Transition-Ctrl
G3, GCs-Ctrl
G4, Transition-cKO
G5, GCs-cKO
G6, Alt-GCs
C
Expression
D Selected Marker Genes
percent.cells
Expression
G1, Pre-GCs
G2, Transition-Ctrl
G4, Transition-cKO
G3, GCs-Ctrl
G5, GCs-cKO
G6, Alt-GCs
Ltbp4
Pear1
Colec11
Car2
Cdh12
Gldn
Col14a1
Cdh13
Myocd
Vcan
Amh
Chn2
Inhba
Tnnc1
Nell2
Pdlim4
Clu
Hsd3b1
E Other Characteristic Genes
percent.cells
Expression
Kitl
Nr5a1
Amhr2
Ano1
Bmp4
Smad3
Inhbb
Apoa4
Top2a
Foxo1
Trp53inp1
Hif1a
Wnt4
Wnt6
Wnt11
Hspd1
Hspe1
Hsph1
Pan-GC
Pre-GC
GC
Hypoxia
Wnt
Hsp
F
gene.ratio
intersection_size
Regulation Of Cell Migration
Regulation Of Lamellipodium Assembly
Homotypic Cell–Cell Adhesion
Protein Localization To Membrane
Semaphorin–Plexin Signaling Pathway
-log10(adj p-value)
N.A.
Endoplasmic Reticulum To Cytosol Transport
Smooth Muscle Cell Differentiation
Retrograde Protein Transport, ER To Cytosol
Positive Regulation Of Integrin–Mediated Signaling Pathway
Regulation Of Basement Membrane Organization
DNA Metabolic Process
Cytoplasmic Translation
Macromolecule Biosynthetic Process
DNA–templated DNA Replication
DNA Replication
Translation
Gene Expression
Mitotic Sister Chromatid Segregation
Negative Regulation Of Chemotaxis
Positive Regulation Of Wnt Signaling Pathway
Negative Regulation Of DNA–templated Transcription
Positive Regulation Of Cell Differentiation
Extracellular Structure Organization
G
Control
Wls cKO
Primordial
Primary
Secondary
Merged
PDLIM4 DDX4 DAPI
PDLIM4

Figure 4

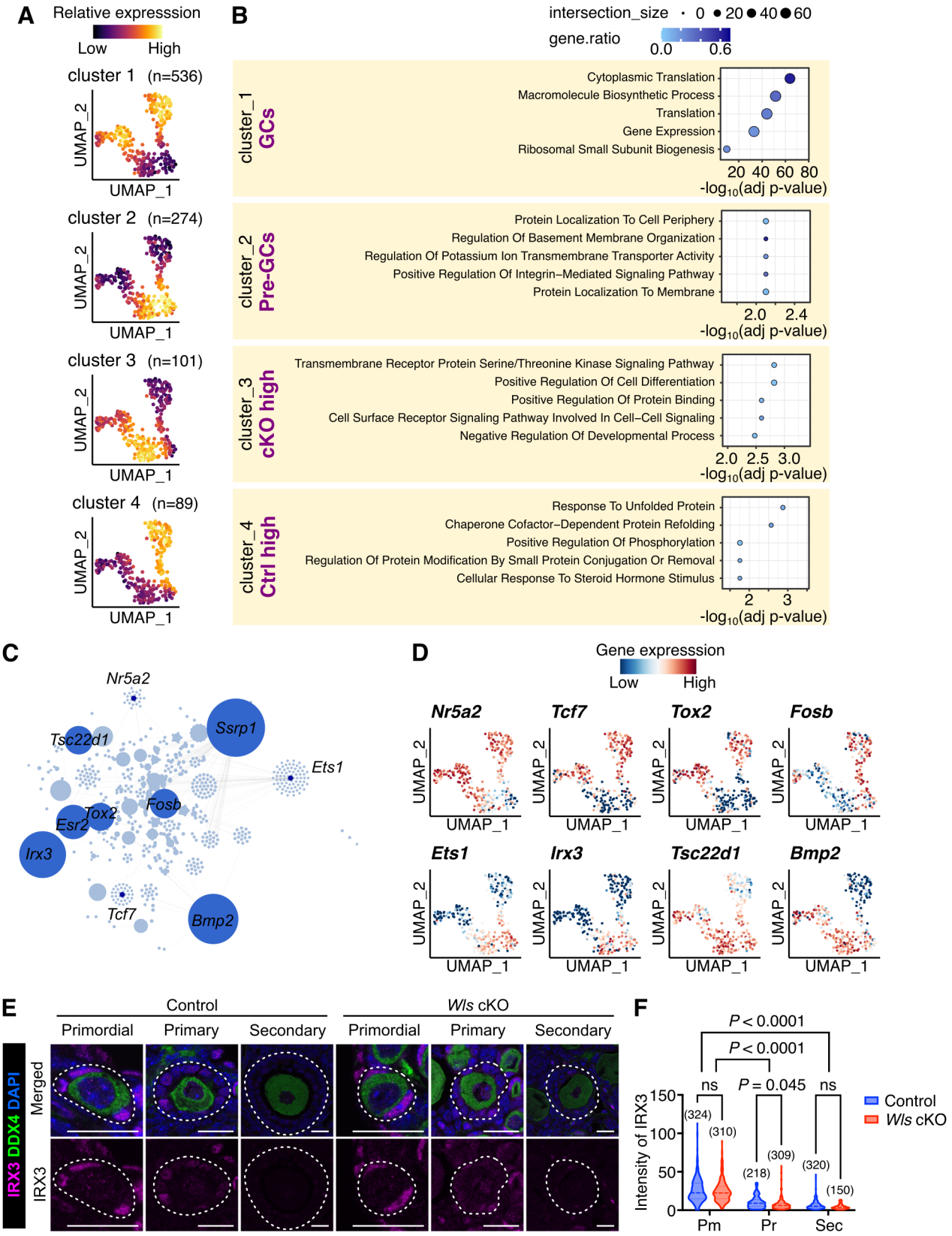
A
Relative expresssion
Low
High
cluster 1 (n=536)
cluster 2 (n=274)
cluster 3 (n=101)
cluster 4 (n=89)
UMAP_2
UMAP_1
B
intersection_size 0 20 40 60
gene.ratio 0.0 0.6
cluster_1 GCs
Cytoplasmic Translation
Macromolecule Biosynthetic Process
Translation
Gene Expression
Ribosomal Small Subunit Biogenesis
20 40 60 80
-log10(adj p-value)
cluster_2 Pre-GCs
Protein Localization To Cell Periphery
Regulation Of Basement Membrane Organization
Regulation Of Potassium Ion Transmembrane Transporter Activity
Positive Regulation Of Integrin–Mediated Signaling Pathway
Protein Localization To Membrane
2.0 2.4
-log10(adj p-value)
cluster_3 cKO high
Transmembrane Receptor Protein Serine/Threonine Kinase Signaling Pathway
Positive Regulation Of Cell Differentiation
Positive Regulation Of Protein Binding
Cell Surface Receptor Signaling Pathway Involved In Cell–Cell Signaling
Negative Regulation Of Developmental Process
2.0 2.5 3.0
-log10(adj p-value)
cluster_4 Ctrl high
Response To Unfolded Protein
Chaperone Cofactor–Dependent Protein Refolding
Positive Regulation Of Phosphorylation
Regulation Of Protein Modification By Small Protein Conjugation Or Removal
Cellular Response To Steroid Hormone Stimulus
2 3
-log10(adj p-value)
C
Nr5a2
Tsc22d1
Ssrp1
Ets1
Tox2
Fosb
Esr2
Irx3
Tcf7
Bmp2
D
Gene expresssion
Low
High
Nr5a2
Tcf7
Tox2
Fosb
Ets1
Irx3
Tsc22d1
Bmp2
UMAP_2
UMAP_1
E
Control
Wls cKO
Primordial
Primary
Secondary
Primordial
Primary
Secondary
IRX3 DDX4 DAPI
Merged
IRX3
F
P < 0.0001
P < 0.0001
ns
P = 0.045
ns
Intensity of IRX3
150
100
50
0
(324)
(310)
(218)
(309)
(320)
(150)
Pm
Pr
Sec
Control
Wls cKO

Figure 5

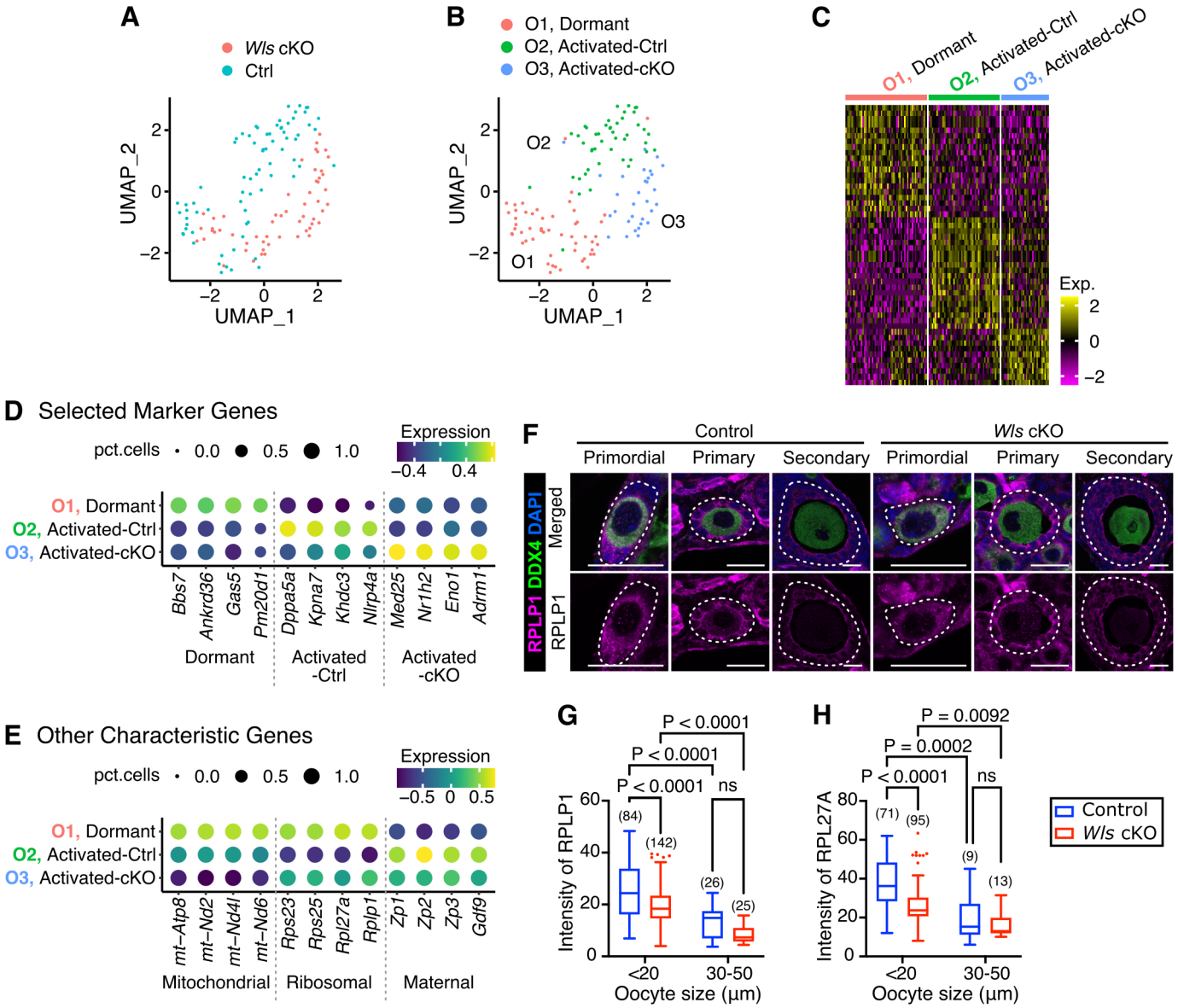
A
Wls cKO
Ctrl
UMAP_2
UMAP_1
B
O1, Dormant
O2, Activated-Ctrl
O3, Activated-cKO
O1
O2
O3
C
O1, Dormant
O2, Activated-Ctrl
O3, Activated-cKO
Exp.
D Selected Marker Genes
pct.cells 0.0 0.5 1.0
Expression
−0.4 0.4
Bbs7
Ankrd36
Gas5
Pm20d1
Dppa5a
Kpna7
Khdc3
Nlrp4a
Med25
Nr1h2
Eno1
Adrm1
Dormant
Activated -Ctrl
Activated -cKO
E Other Characteristic Genes
pct.cells 0.0 0.5 1.0
Expression
−0.5 0 0.5
mt−Atp8
mt−Nd2
mt−Nd4l
mt−Nd6
Rps23
Rps25
Rpl27a
Rplp1
Zp1
Zp2
Zp3
Gdf9
Mitochondrial
Ribosomal
Maternal
F
Control
Wls cKO
Primordial
Primary
Secondary
RPLP1 DDX4 DAPI
Merged
RPLP1
G
P < 0.0001
P < 0.0001
P < 0.0001
ns
Intensity of RPLP1
(84)
(142)
(26)
(25)
<20
30-50
Oocyte size (μm)
H
P = 0.0092
P = 0.0002
P < 0.0001
ns
Intensity of RPL27A
(71)
(95)
(9)
(13)
Control
Wls cKO

Figure 6

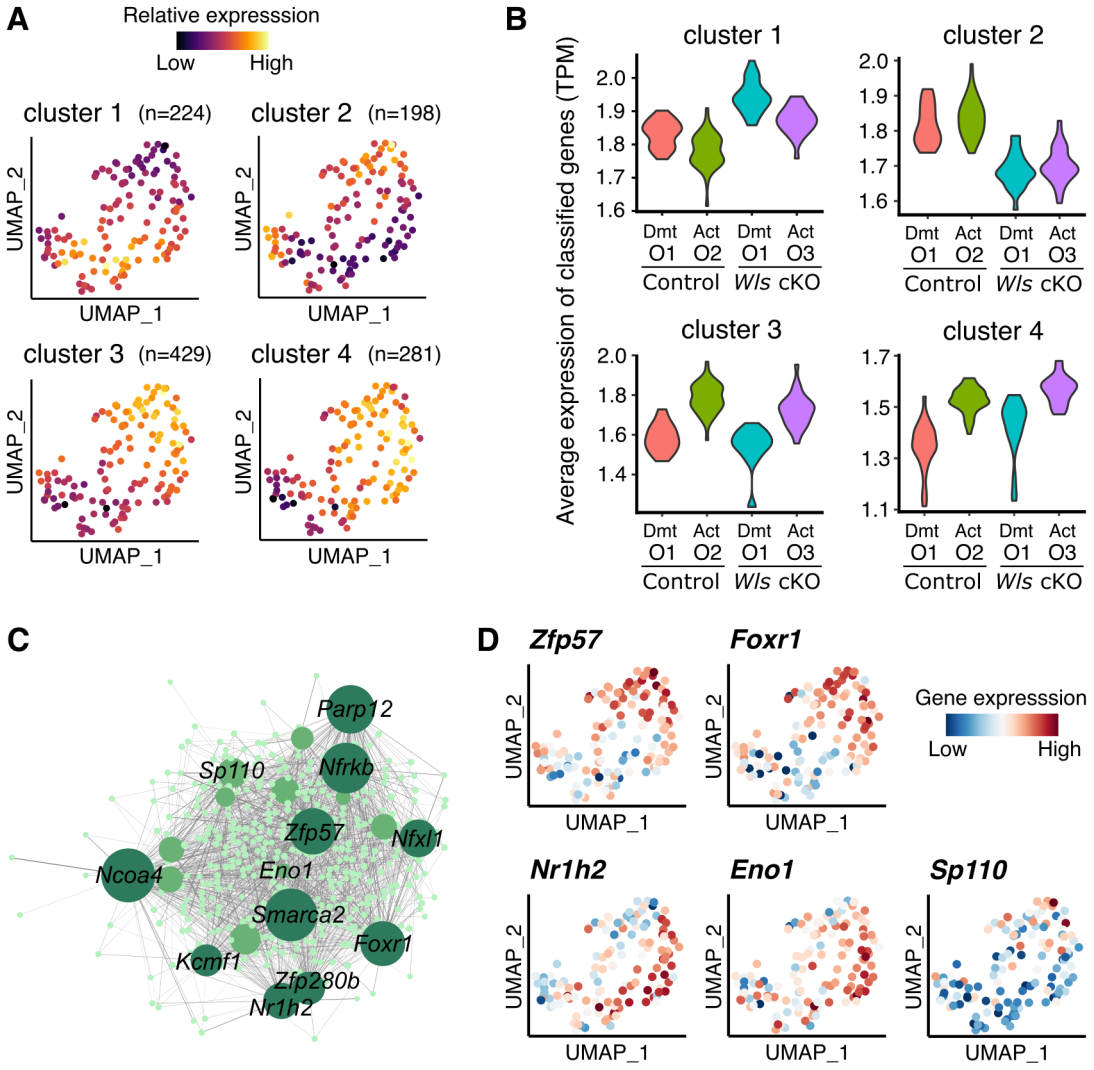
A
Relative expresssion
Low
High
cluster 1 (n=224)
cluster 2 (n=198)
cluster 3 (n=429)
cluster 4 (n=281)
UMAP_2
UMAP_1
B
Average expression of classified genes (TPM)
cluster 1
cluster 2
cluster 3
cluster 4
Dmt O1
Act O2
Dmt O1
Act O3
Control
Wls cKO
C
Parp12
Sp110
Nfrkb
Zfp57
Nfxl1
Ncoa4
Eno1
Smarca2
Foxr1
Kcmf1
Zfp280b
Nr1h2
D
Zfp57
Foxr1
Gene expresssion
Low
High
Nr1h2
Eno1
Sp110

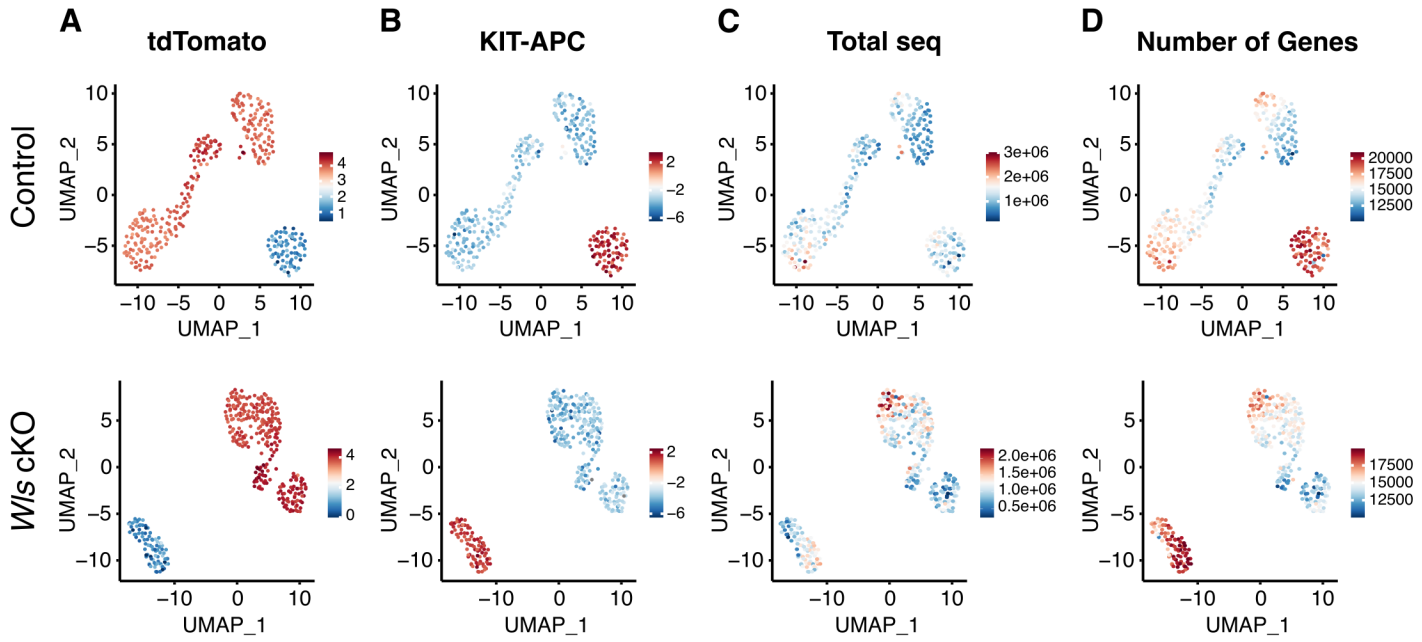

Fig S1. Optical detection of cells and quality control for single-cell RNA sequencing. UMAP plots showing tdTomato-expressing somatic cells (**A**), the KIT-APC positive oocyte population (**B**), the total number of mapped reads (total seq) (**C**), and the number of detected genes (number of genes) (**D**). The color scale represents the gene expression level scaled by the Z-score.

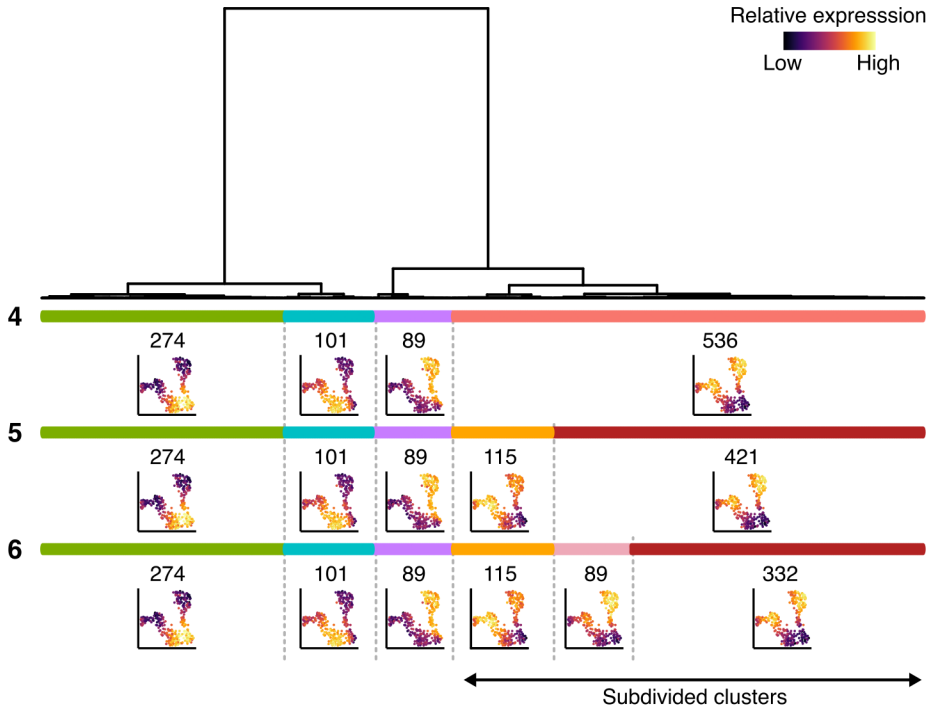

Fig S2. DEG clustering dendrogram of GC populations based on expression kinetics. Diagram of hierarchical clustering based on the kinetics of DEGs obtained by the singleCellHaystack method in the GC population. Color bars represent the clustering result when the dendrogram is cut into 4-6 clusters. The number to the left of each bar indicates the number of clusters. The average expression levels of the genes in each cluster were projected onto UMAP plots below the corresponding bars. More clusters lead to a greater

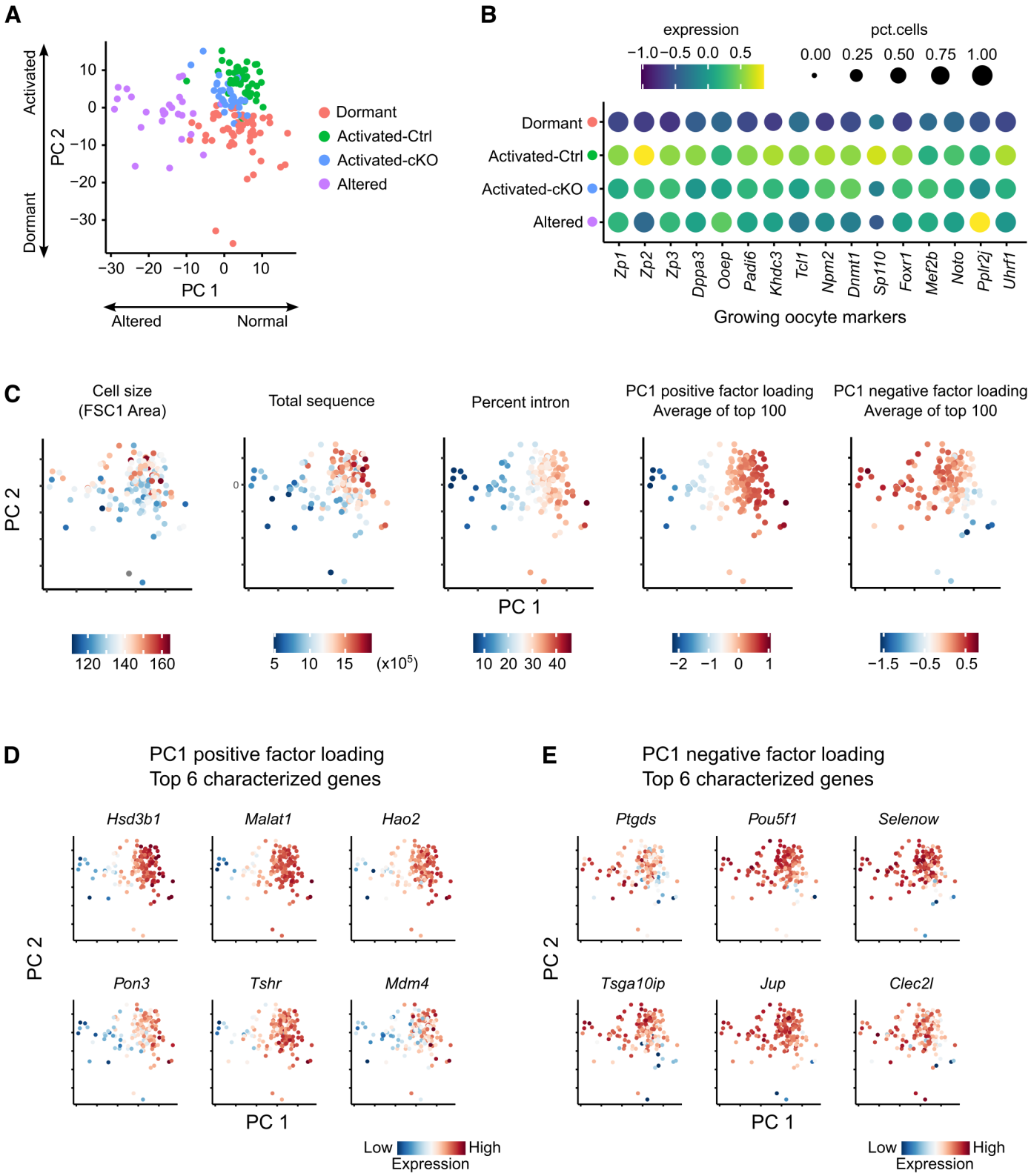

Fig S3. Characteristic features of the altered-oocyte subcluster. (**A**) PCA plots of oocytes. Different colors correspond to subclusters of oocytes. The principal components on the axes capture the major sources of gene expression variation, with their respective contributions indicated in the axis labels. (**B**) Dot plot showing the expression of growing oocyte markers. The dot size represents the ratio of cells expressing a specific marker (TPM > 1), while the color indicates the average gene expression level scaled by the Z-score. (**C**) UMAP plots showing cell size, the total number of mapped reads (total sequence), the ratio of intronic reads (percent intron), the PC1 positive factor loading and the PC1 negative factor loading. (**D**) UMAP plots showing the top 6 characterized genes of PC1 positive factor loading. (**E**) UMAP plots showing the top 6 characterized genes of PC1 negative factor loading.

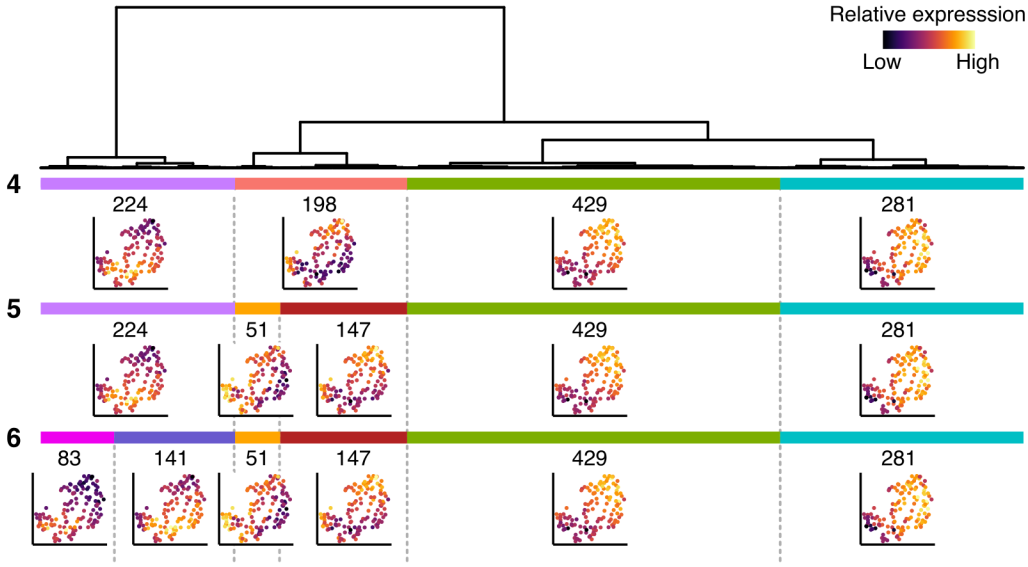

Fig S4. DEG clustering dendrogram of oocyte populations based on expression kinetics similarity. Diagram of hierarchical clustering based on the kinetics of DEGs obtained by the singleCellHaystack method in the oocyte population. Color bars represent the clustering result when the dendrogram is cut into 4-6 clusters. The number on the left of each bar indicates the number of clusters. The average expression level of the genes in each cluster were projected onto UMAP plots below the corresponding bars.